Entanglement generation in periodically driven integrable systems: dynamical phase transitions and steady state

Arnab Sen, Sourav Nandy, and K. Sengupta
Department of Theoretical Physics, Indian Association for the Cultivation of Science, Jadavpur, Kolkata 700032, India.
(Dated: August 9, 2016)

We study a class of periodically driven $d-$dimensional integrable models and show that after n drive cycles with frequency ω, pure states with non-area-law entanglement entropy $S_n(l) \sim l^{\alpha(n,\omega)}$ are generated, where l is the linear dimension of the subsystem, and $d-1 \leq \alpha(n,\omega) \leq d$. We identify and analyze the crossover phenomenon from an area ($S \sim l^{d-1}$ for $d \geq 1$) to a volume ($S \sim l^d$) law and provide a criterion for their occurrence which constitutes a generalization of Hastings' theorem to driven integrable systems in one dimension. We also find that S_n generically decays to S_∞ as $(\omega/n)^{(d+2)/2}$ for fast and $(\omega/n)^{d/2}$ for slow periodic drives; these two dynamical phases are separated by a topological transition in the eigensprectrum of the Floquet Hamiltonian. This dynamical transition manifests itself in the temporal behavior of all local correlation functions and does not require a critical point crossing during the drive. We find that these dynamical phases show a rich re-entrant behavior as a function of ω for $d = 1$ models, and also discuss the dynamical transition for $d > 1$ models. Finally, we study entanglement properties of the steady state and show that singular features (cusps and kinks in $d = 1$) appear in S_∞ as a function of ω whenever there is a crossing of the Floquet bands. We discuss experiments which can test our theory.

PACS numbers:

arXiv:1511.03668v3 [cond-mat.str-el] 8 Aug 2016

I. INTRODUCTION

Entanglement entropy of a correlated many-body system has been the subject of intense theoretical study in recent years[1,2]. It is well-known that this quantity, which probes non-local correlations of a quantum many-body state, may serve as an indicator of topological properties of correlated ground states of several systems such as spin-liquids[1], quantum Hall systems[3], symmetry broken systems[4], interacting fermions[5] and topological insulators[6]. In addition, it also contains information about universal features of quantum phase transitions and serves as an indicator of a topological quantum phase transition where the absence of a local order parameter renders the usual Landau description of the transition impossible[7,8]. More recently, entanglement entropy for ground states of conformal and/or large N field theories have received a lot of attention both from a field theory perspective[9,10] as well as from the perspective of their gravity duals in an AdS background[11].

In most cases, the computation of entanglement entropy involves computing the reduced density matrix of a quantum many-body system and/or interacting field theories. This is usually done by starting from the density matrix corresponding to the quantum ground state, followed by division of the system into a subsystem of linear dimension l and "environment" of linear dimension $L-l$, where L is the system size. One then integrates out the degrees of freedom which belong to the environment and obtains the reduced density matrix ρ_r for the subsystem. The entanglement entropy can then be computed from ρ_r by using one of the possible measures

$$\begin{aligned} S_n &= (1-n)^{-1}\mathrm{Tr}[\rho_r^n] \\ S &= -\mathrm{Tr}[\rho_r \ln \rho_r] = \lim_{n\to 1} S_n, \end{aligned} \tag{1}$$

where S_n is the n^{th} Rényi entropy and S denotes the Von-Neumann entanglement entropy. Such a quantity measures the entanglement of the subsystem with rest of the system. It is well known that for a generic short-ranged Hamiltonian, S is controlled by the boundary between the subsystem and environment leading to

$$S \sim l^{d-1} \quad d \geq 1. \tag{2}$$

In one dimension, the area law behavior of ground states with local Hamiltonians and gapped spectrum has been proven and also goes by the name of Hastings' theorem[12] ($d = 1$ critical points have a further multiplicative logarithmic correction, i.e., $S \sim \ln l$). It is believed that ground states of local Hamiltonians in higher dimensions show an analogous area law behavior[13]. More recently, the subleading terms in the expression of entanglement entropy have been carefully studied[1]. Such studies yield $S \sim l^{d-1} + \Gamma$ (for $d > 1$). The subleading factor Γ, when non-zero, encodes the topological character of the ground state of the system and is often refereed to as the topological entanglement entropy. We note here that the boundary-law for the entanglement entropy encoded in Eq. 2 is surprisingly robust. In fact, the only known violation for an area law for quantum ground states (apart from critical points in $d = 1$) occur for systems with gapless Fermi surface in $d > 1$ where the correlation functions of local operators become long-ranged leading to $S \sim l^{d-1} \ln l$. However, it is known that other states in the Hilbert space of a quantum system which are not the ground state of the local Hamiltonian describing the system may have non-area law behavior for the entanglement entropy. A class of these states, obey the volume law, namely, $S \sim l^d$ for a $d-$ dimensional quantum system.

There have been several studies in recent past on non-equilibrium dynamics of closed quantum systems[14–17].

Such studies initially focused on behavior of the system following quench and ramp dynamics. A class of these studies dealt with the behavior of such systems following a ramp through a second order phase transition and discussed the presence/absence of Kibble-Zurek scaling and their extensions[14,15,18–20]. The other class focused on long-time behavior of these systems following a quench and the character of the steady states they attain[21]. Such studies are mainly motivated by presence of experimental platforms in the form of ultracold atom systems where relevant experiments can be carried out[22]. More recently, the properties of periodically closed driven quantum systems which involved multiple passage through an intermediate quantum critical point has received a lot of attention; in particular such dynamics has been shown to lead to interesting phenomenon such as dynamic freezing[23,24] and to novel steady states[25]. Moreover, such driven systems are known to undergo dynamic phase transitions which manifests itself in cusp like behavior of the Loschmidt echo and can be understood as a consequence of the non-analyticities (Fischer zeroes) of the dynamical free energy of the driven systems[26–29].

The properties of entanglement entropy for states resulting from non-equilibrium dynamics of closed quantum system has also received some attention in recent years. The initial studies in this direction focused on integrable spin-models and on single/two-spin entanglement[30,31]. Later, there have been several studies on the entanglement properties of quantum systems right after a ramp through a critical point[32] and on evolution of entanglement entropy after a sudden quench[33]. The first class of study did not find violation of the area-law behavior while the second class of study found ballistic spread of entanglement entropy followed by a plateau where it attains a constant value at long times. This constant value S_f follows volume law ($S_f \sim l^d$) and thus one sees a crossover from an area to a volume law as a result of the dynamics. Such a spread has also been studied in the context of integrable spin models where the system is allowed to evolve after being driven periodically; an analogous growth of entanglement entropy leading to a volume law was also observed for such protocols[34]. However, to the best of our knowledge, the fate of the entanglement entropy of a periodically driven quantum system, where the drive generates multiple passage of the system through an intermediate quantum critical point, has not been studied so far. In particular, the crossover of entanglement entropy from an area to a volume law behavior as a function of drive frequency ω and number of drive cycles n has not been investigated in this context. The convergence of the reduced density matrix of a subsystem to the final ($n \to \infty$) steady state density matrix has also not been explored for a periodically driven system.

In this work we aim to fill up this gap in the literature by studying a class of integrable models subjected to a periodic drive with frequency ω for n cycles whose Hamiltonian is given by

$$H = \sum_{\vec{k}} \psi^\dagger_{\vec{k}} \left[(g(t) - b_{\vec{k}})\tau_3 + \Delta_{\vec{k}}\tau_1 \right] \psi_{\vec{k}}, \tag{3}$$

where $\vec{k}$ is $d-$dimensional momentum vector, $\psi_{\vec{k}} = (c_{\vec{k}}, c^\dagger_{-\vec{k}})^T$, $c_{\vec{k}}$ denotes fermionic annihilation operator, τ_3 and τ_1 are Pauli matrices, and $g(t)$ is a periodic function of time. Such Hamiltonians constitute fermionic representations of Ising and XY models in $d = 1$, the Kitaev model in $d = 2$[19,36–40], and Dirac quasiparticles of graphene and atop topological insulator surfaces[41,42]. The relation of Eq. 3 to Ising and Kitaev models has been charted out in Appendix A. In what follows, we shall study the entanglement entropy $S_n(l)$ (with l denoting the linear dimension of the subsystem) of a system described by Eq. 3 after n drive cycles with frequency ω.

The main results of our study are as follows. First, we find that for a generic n (and also in the $n \to \infty$ limit where the system's state is described by the diagonal ensemble) and ω, $S_n \sim l^{\alpha(n,\omega)}$, where $\alpha(n,\omega)$ satisfies $d-1 \leq \alpha(n,\omega) \leq d$; thus a periodic drive may be used to generate states with non-area-law entanglement entropy in a controlled manner. We construct a Hamiltonian $\mathcal{H}_t$ for which the state obtained after n drive cycles is the ground state and show that the crossover of S_n from an area to a non-area law can be related to the short-/long-range nature of $\mathcal{H}_t$; our analysis in this regard constitutes a generalization of Hastings' theorem to driven $d = 1$ integrable quantum systems. Second, we show that such periodically driven systems show two distinct dynamical phases when the driving frequency is varied; S_n relaxes to its steady state value S_∞ as $(\omega/n)^{(d+2)/2}[(\omega/n)^{d/2}]$ in the former [latter] phase which corresponds to fast [slow] ω. These two phases are separated by a transition occurring at a critical drive frequency ω_c which involves change in topology of spectrum of the system's Floquet Hamiltonian H_F. Third, we show that these phases exhibit reentrant behavior as a function of ω for $d = 1$. We provide a generic phase diagram for this phenomenon as a function of the drive frequency and amplitude for the 1D Ising model. We also provide an analytical expression for the phase boundary for periodic kick protocol which matches the numerical results accurately. We discuss the nature of this transition in $d = 2$ models and point out some essential differences compared to the $d = 1$ case. We demonstrate that the dynamic phase transition unraveled here is of fundamentally different origin from the class of transitions studied in Refs. 26–29 and point out the essential difference between the two. Finally, we study S_∞, as obtained from the steady state (diagonal ensemble), as a function of ω and show the presence of singularities in S_∞ (cusps and kinks in $d = 1$) that are universal features directly related to the crossing of Floquet bands obtained from the time evolution operator $U(T)$ for one complete driving period T. We discuss experiments which can test our theory.

The plan of the rest of the work is as follows. In Sec.

II, we numerically demonstrate the area- to volume-law crossover of S and chart out the construction of H_t. This is followed by Sec. III, where we discuss the dynamical transition reflected in relaxation of S_n and various local quantities and relate such behavior to the properties of the Floquet spectrum of the driven system. Next, we discuss the behavior of the steady state entanglement entropy S_∞ as a function of the drive frequency in Sec. IV. Finally, we discuss our results, chart out possible experiments which can test them, and conclude in Sec. V. Some details of calculations are shown in the appendices.

II. AREA- TO VOLUME-LAW CROSSOVER

We begin this section with a brief sketch of our method for computing S_n numerically. In what follows, we vary $g(t)$ (Eq. 3) periodically in time. Although most of our results would be protocol independent, for numerical purposes, unless mentioned otherwise, we use the square pulse drive protocol:

$$\begin{aligned} g(t) &= g_i, \quad (n-1)T \le t \le (n-1/2)T \\ &= g_f, \quad (n-1/2)T \le t \le nT, \end{aligned} \tag{4}$$

where $T = 2\pi/\omega$ is the time period. The issue of protocol independence of some of our results is charted out in further detail in Appendix B. To solve the dynamics, we define the annihilation operators $\gamma_k(t)$:

$$\gamma_{\vec{k}} = u_{\vec{k}}(t) c_{\vec{k}} + v^*_{\vec{k}}(t) c^\dagger_{-\vec{k}}. \tag{5}$$

Here $u_{\vec{k}}(t)$ and $v_{\vec{k}}(t)$ satisfy the Schrödinger equation

$$i\partial_t |\psi_{\vec{k}}\rangle = H_{\vec{k}}(t) |\psi_{\vec{k}}\rangle, \tag{6}$$

where $|\psi_{\vec{k}}\rangle = (u_{\vec{k}}, v_{\vec{k}})^T$ and we have set $\hbar = 1$. The wavefunction $|\psi(t)\rangle$ of the entire system equals

$$\begin{aligned} |\psi(t)\rangle &= \otimes_{\vec{k}\in \mathrm{BZ}/2} |\psi_{\vec{k}}(t)\rangle \\ |\psi_{\vec{k}}(t)\rangle &= u_{\vec{k}}(t) c^\dagger_{\vec{k}} c^\dagger_{-\vec{k}} |0\rangle + v_{\vec{k}}(t) |0\rangle \end{aligned} \tag{7}$$

where $\vec{k}$ is taken over half of the Brillouin zone (BZ) and $|0\rangle$ denotes the vacuum of the c fermions.

Having obtained $|\psi_{\vec{k}}(nT)\rangle$, the calculation of S_n requires the construction of two $l^d \times l^d$ matrices[43], $\mathbf{C}$ and $\mathbf{F}$, whose elements can be constructed by knowing $u_k(t)$ and $v_k(t)$ after n drive period:

$$\begin{aligned} C_{ij} &= \langle c^\dagger_{\vec{i}} c_{\vec{j}} \rangle_n = 2 \sum_{\vec{k}\in \mathrm{BZ}/2} |u_{\vec{k}}(t)|^2 \cos(\vec{k}\cdot(\vec{i}-\vec{j}))/L^d \\ F_{ij} &= \langle c^\dagger_{\vec{i}} c^\dagger_{\vec{j}} \rangle_n = 2 \sum_{\vec{k}\in \mathrm{BZ}/2} u^*_{\vec{k}}(t) v_{\vec{k}}(t) \sin(\vec{k}\cdot(\vec{i}-\vec{j}))/L^d \end{aligned} \tag{8}$$

where i, j refer to sites in the subsystem. Using these expressions, we construct the $2l \times 2l$ matrix $\mathcal{C}_n(l)$ given by

$$\mathcal{C}_n(l) = \begin{pmatrix} \mathbf{I}-\mathbf{C} & \mathbf{F} \\ \mathbf{F}^* & \mathbf{C} \end{pmatrix}. \tag{9}$$

S_n can then be obtained from $2l$ eigenvalues p_i of $\mathcal{C}_n(l)$: $S_n(l) = -\mathrm{Tr}[\rho_r \ln \rho_r] = -\sum_{i=1}^{2l} p_i \log(p_i)$, where ρ_r is the subsystem density matrix after n drive cycles[43]. The details of this calculation is sketched in Appendix C.

The result of such a numerical study is shown in Fig. 1. In Fig. 1(a), we plot $S_n(l)$ as a function of l for $d = 1$ Ising model and several n. From this plot, we find that the minimum value of l beyond which $S_n(l)$ satisfies the area law (i.e., $S_n(l) \sim$ constant in $d = 1$) diverges as $n \to \infty$ leading to genuine non-area scaling. In this regime, $S_n(l) \sim l^{\alpha(n,\omega)}$ where $d - 1 \le \alpha(n,\omega) \le d$. The $n \to \infty$ result is reproduced by the Diagonal Ensemble; and we detail those calculations in Sec. IV. Next, as shown in Fig. 1(b), we find that $S_n(l)$ grows linearly as a function of n for a fixed l and then attains a constant (l dependent) value; this behavior is qualitatively similar to the linear spread of S following a quench[33].

To understand how fast the volume law is approached in the steady state (Diagonal ensemble) for a certain drive protocol for different l, we define the estimator

$$\alpha(l) = \log[S_\infty(2l)/S_\infty(l)]/\log(2), \tag{10}$$

and plot it as a function of l for several representative ω in Fig. 2. In 1D, $\alpha \to 0(1)$ if area(volume)-law is satisfied. We find a rapid and monotonic convergence of α to unity for large ω. In contrast, for small ω, this convergence is quite slow and has non-monotonic features. Thus, periodic drives at small ω offer a route to stabilizing pure quantum states with non-area and non-volume scaling of S_n[44].

These results lead to the natural question regarding the area-law behavior for a finite l and n; in particular, it seems desirable to have an analytical criterion which may, at least qualitatively predict that area or non-area law behavior of S as a function of l for a given n. We attempt to provide such a criterion below. To this end, we construct $\mathcal{H}_{\vec{k}t}$ for which $|\psi_{\vec{k}}(nT)\rangle$ generated after n drive cycles is the ground state. The motivation for doing this is as follows. From Hastings' theorem, the ground state of a local Hamiltonian in one dimension yields S which exhibits area law[12]. For a driven integrable system, S_∞ is expected to be described by a Generalized Gibbs Ensemble (GGE), and thus to follow volume-law[33]. Thus after n cycles of the drive, for (small)large n, one expects $\mathcal{H}_{\vec{k}t}$ to be short(long) ranged and the crossover between short- to long-range behavior of $\mathcal{H}_{\vec{k}t}$ for a given l might provide an indication of the numerically observed area- to volume-law crossover of S_n.

To construct $\mathcal{H}_{\vec{k}t}$ we start from $\psi_k(t_f = nT)$ and seek a solution of

$$\mathcal{H}_{\vec{k}t} = \epsilon_{\vec{k}t}\tau_3 + \Delta_{\vec{k}t}\tau^+ + \Delta^*_{\vec{k}t}\tau^-, \tag{11}$$

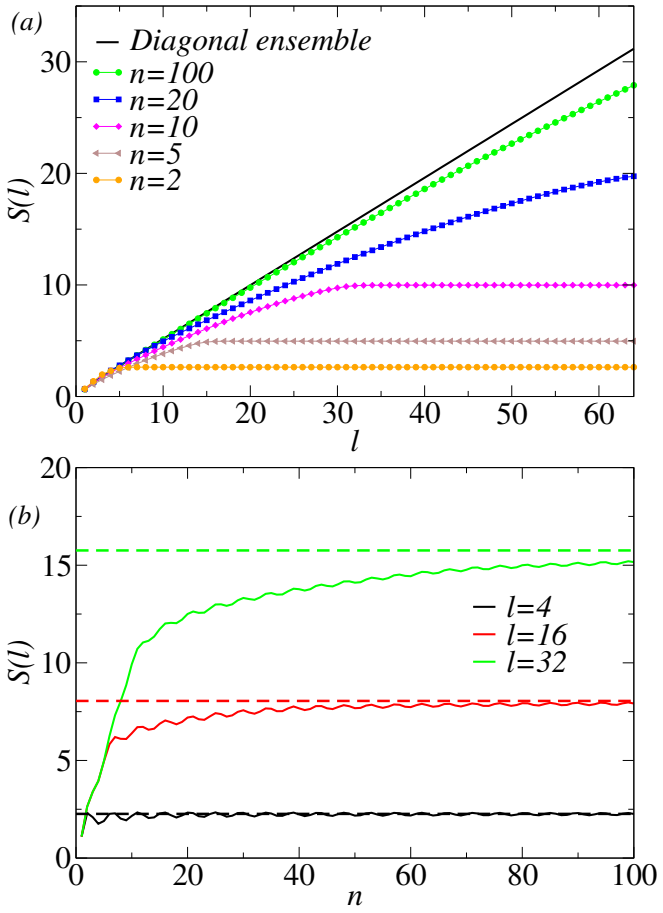

FIG. 1: S_n for 1D Ising model for which $\Delta_k = \sin(k)$, $b_k = \cos(k)$ and $J = 1$. The transverse field $h(t) = g(t)$ follows the square pulse protocol ($g_i = 2$ and $g_f = 0$), and the ground state at $g_i = 2$ is taken to be the starting state. (a) S_n versus l for several n and $\omega = \pi$ (b) S_n versus n for several l and $\omega = \pi$.

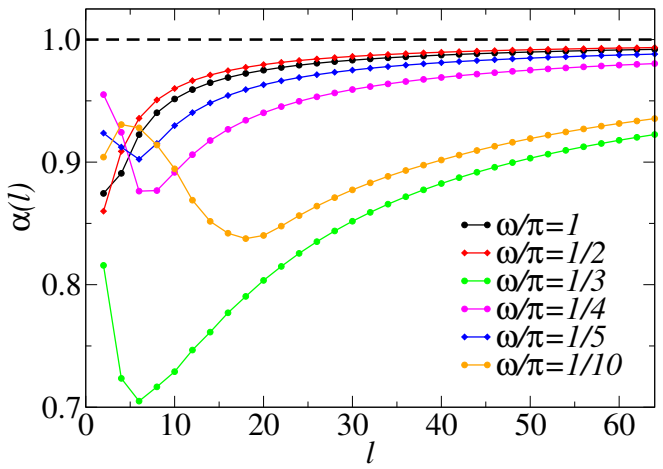

FIG. 2: Behavior of $\alpha(l)$ versus l (Eq. 10) in the steady state for several ω (square pulse protocol with $g_i = 2$ and $g_f = 0$) for the 1D Ising model.

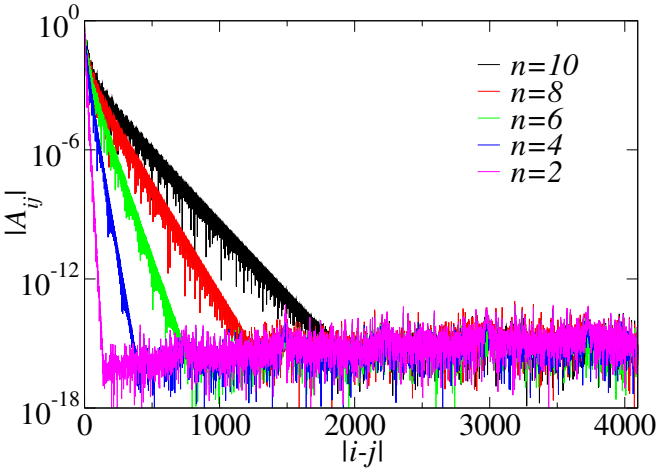

FIG. 3: $|A_{ij}|$ versus $r = |i - j|$ for several n and $\omega = 2\pi$ for 1D ising model where the transverse field $h(t) = g(t)$ follows the square pulse protocol ($g_i = 2$ and $g_f = 0$).

which satisfies

$$\mathcal{H}_{\vec{k}t}\psi_{\vec{k}}(t_f) = -(\epsilon_{\vec{k}t}^2 + |\Delta_{\vec{k}t}|^2)^{1/2}\psi_{\vec{k}}(t_f). \quad (12)$$

Assuming that $\mathcal{H}_{\vec{k}t} \simeq H_{\vec{k}}$ in the adiabatic limit, we find, after some straightforward algebra,

$$\begin{aligned} \epsilon_{\vec{k}t} &= \Delta_{\vec{k}}(|u_{\vec{k}}(t_f)|^2 - |v_{\vec{k}}(t_f)|^2)/(2|u_{\vec{k}}(t_f)||v_{\vec{k}}(t_f)|) \\ \Delta_{\vec{k}t} &= \Delta_{\vec{k}}\exp(i(\alpha_{\vec{k}} - \beta_{\vec{k}})) \end{aligned} \quad (13)$$

where we have defined $\alpha_{\vec{k}}(\beta_{\vec{k}}) = \mathrm{Arg}[u_{\vec{k}}(t_f)(v_{\vec{k}}(t_f))]$. The real-space form of the effective Hamiltonian is given by Fourier transform of $\mathcal{H}_{\vec{k}t}$

$$\mathcal{H}_t = \sum_{\vec{ij}}(A_{\vec{i}-\vec{j}}c_{\vec{i}}^\dagger c_{\vec{j}} + B_{\vec{i}-\vec{j}}c_{\vec{i}}c_{\vec{j}} + \text{h.c.}), \quad (14)$$

where $A_{\vec{ij}}$ and $B_{\vec{ij}}$ are Fourier transforms of $\epsilon_{\vec{k}t}$ and $\Delta_{\vec{k}t}$ respectively. A plot of $|A_{ij}|$ as a function of $|i - j|$ for the $d = 1$ Ising model (Fig. 3), shows $A_{ij} \sim \exp[-|i - j|/R_t(n, \omega)]$; this indicates that $\mathcal{H}_t$ appears short-ranged in the length scale $l \gg R_t(n, \omega)$ and long-ranged for $l \ll R_t(n, \omega)$. As shown in Fig. 3, $R_t(n, \omega)$ increases rapidly with n; we find numerically that for $l \gg (\ll) R_t(n, \omega)$, S_n follows area(non-area)-law in accordance with Hastings' theorem. This result constitutes a generalization of Hastings' theorem for driven integrable models.

Before ending this section, we note that the deduction of nature of S from that of $\mathcal{H}_t$ involves two scales. The first constitutes the minimal subsystem size $l_{\min}$ below which the subsystem shows a non-area law behavior for a given n while the second is $R_t(n, \omega)$ which determines the effective long-raged or short-ranged nature of $\mathcal{H}_t$ with respect to l. We find numerically that $R_t(n, \omega)$ shows a much faster growth with n than $l_{\min}$; thus whereas we do find that $R_t(n, \omega) \gg l$ and $R_t(n, \omega) \ll l$ correspond to two different behaviors of $S(l)$ as a function of l, it

is generally not possible to identify $R_t(n,\omega) \sim l$ as the point of crossover of $S(l)$ from one type of behavior to the other type.

III. DYNAMICAL TRANSITION AND PHASE DIAGRAM

In this section we first study the relaxation behavior of the local quantities in the system to their steady state values and unravel a dynamic transition in this relaxation behavior as a function of drive frequency ω in Sec. III A for both $d = 1$ (Sec. III B) and $d = 2$ (Sec. III C). This is followed by numerical and analytical study of the corresponding phase diagram for 1D transverse field Ising model for square and kicked pulse protocol in Sec. III D to illustrate the rich re-entrant behavior as a function of ω in $d = 1$.

A. Relaxation of S_n

To study the relaxation of S_n to S_∞, we define a distance measure which provides us information regarding this relaxation as a function of n, and also of the relaxation of the local density matrix ρ_r (and hence all local quantities within that subsystem) to the final Diagonal Ensemble result. For integrable models S_n is determined by the two-point correlators $\mathcal{C}_n(l)$; thus it is natural to define[45]

$$\mathcal{D} = \mathrm{Tr}[(\mathcal{C}_\infty(l) - \mathcal{C}_n(l))^\dagger(\mathcal{C}_\infty(l) - \mathcal{C}_n(l))]^{1/2}/(2l). \quad (15)$$

We note that $0 \leq \mathcal{D} \leq 1$ and it vanishes only if $C_n = C_\infty$. The details of its calculation is given in Appendix D. We find numerically for the square pulse protocol (Figs. 4 (a), (b), and (c) and 5(a)) that for both $d = 1$ Ising and $d = 2$ Kitaev models, $\mathcal{D}$ exhibits two distinct behaviors corresponding to different dynamical regimes: $\mathcal{D} \sim (\omega/n)^{(d+2)/2}[(\omega/n)^{d/2}]$ in these two regimes. For the drive amplitude used in Fig. 4 we also find that these two dynamical regimes are separated by re-entrant transitions at $\omega_c = 1.16\pi$, 0.47π, and 0.42π for the $d = 1$ Ising model; however, for $d = 2$ Kitaev model, there is a single such transition $\omega_c = 4.01\pi$[46].

To understand the origin of this transition, we analyze the Floquet Hamiltonian H_F for the driven system. After n drive cycles, the wavefunction is given by

$$\begin{aligned} |\psi_{\vec{k}}(t = nT)\rangle &= U_{\vec{k}}^n |\psi_{\vec{k}}(t = 0)\rangle \\ &= \exp[-inH_{\vec{k}F}T]|\psi(t = 0)\rangle, \end{aligned} \quad (16)$$

where $H_{\vec{k}F}$ is the Floquet Hamiltonian of the system for the wavevector $\vec{k}$[47], $H_F = \sum_{\vec{k}} H_{\vec{k}F}$, and $U_{\vec{k}}$ is given by

$$U_{\vec{k}} = \cos(\theta_{\vec{k}}) \exp[i\alpha_{\vec{k}}\tau_3] - i\tau_2 \sin(\theta_{\vec{k}}) \exp[i\gamma_{\vec{k}}\tau_3]. \quad (17)$$

The parameters $\theta_{\vec{k}}$, $\alpha_{\vec{k}}$ and $\gamma_{\vec{k}}$ can be expressed in terms of the initial and final wavefunctions; for example for $|\psi_{\vec{k}}(t = 0)\rangle = (0, 1)^T$ and $|\psi_{\vec{k}}(t = T)\rangle = (u_{\vec{k}f}, v_{\vec{k}f})^T$, one has $\sin(\theta_{\vec{k}}) = |u_{\vec{k}f}|$, $\alpha_{\vec{k}} = -\mathrm{Arg}(v_{\vec{k}f})$ and $\gamma_{\vec{k}} = \mathrm{Arg}(u_{\vec{k}f})$. We further note that $U_{\vec{k}}$ becomes diagonal at the edge and center of the BZ where $\Delta_{\vec{k}} = 0$ leading to $\sin(\theta_{\vec{k}}) = 0$ at these points. More details of these calculations can be found in Appendix E.

To obtain $H_{\vec{k}F}$, we note that the unitary nature of $U_{\vec{k}}$ guarantees that $H_{\vec{k}F}$ can be expressed in terms of the Pauli matrices. This allows us to write

$$H_{\vec{k}F} = \vec{\sigma} \cdot \vec{\epsilon}_{\vec{k}} = |\vec{\epsilon}_{\vec{k}}|\vec{\sigma} \cdot \hat{n}_{\vec{k}} \quad (18)$$

where $\vec{\epsilon}_{\vec{k}} = (\epsilon_{\vec{k}1}, \epsilon_{\vec{k}2}, \epsilon_{\vec{k}3})$, and $\hat{n}_{\vec{k}i} = \epsilon_{\vec{k}i}/|\vec{\epsilon}_{\vec{k}}|$. Here the quasienergies $\epsilon_{\vec{k}i}$ are given by

$$\begin{aligned} \epsilon_{1\vec{k}} &= -|\vec{\epsilon}_{\vec{k}}| \sin(\theta_{\vec{k}}) \sin(\gamma_{\vec{k}}) \sin(T|\epsilon_{\vec{k}}|)/D_{\vec{k}} \\ \epsilon_{2\vec{k}} &= -|\vec{\epsilon}_{\vec{k}}| \sin(\theta_{\vec{k}}) \cos(\gamma_{\vec{k}}) \sin(T|\epsilon_{\vec{k}}|)/D_{\vec{k}} \\ \epsilon_{3\vec{k}} &= -|\vec{\epsilon}_{\vec{k}}| \cos(\theta_{\vec{k}}) \sin(\alpha_{\vec{k}}) \sin(T|\epsilon_{\vec{k}}|)/D_{\vec{k}} \\ D_{\vec{k}} &= \sqrt{1 - \cos^2(\theta_{\vec{k}}) \cos^2(\alpha_{\vec{k}})}. \end{aligned} \quad (19)$$

Thus one can write

$$U_{\vec{k}} = \exp[-i(\vec{\sigma} \cdot \hat{n}_{\vec{k}})\phi_{\vec{k}}], \quad (20)$$

where $\phi_{\vec{k}} = T|\vec{\epsilon}_{\vec{k}}|$. We work in the reduced zone scheme where $\phi_{\vec{k}} \in [0, \pi]$ and each of the component of $\vec{\epsilon}_{\vec{k}}$ is restricted to $[-\pi/T, \pi/T]$. We note that from the above structure it is clear that $n_{1\vec{k}} = n_{2\vec{k}} = 0$ and $n_{3\vec{k}} = \pm 1$ at the edge and center of the BZ where $U_{\vec{k}}$ is diagonal; at all other point in the BZ, all three components of $\vec{n}_{\vec{k}}$ are generally non-zero. Using Eq. 17, one can then obtain the Floquet spectrum

$$|\vec{\epsilon}_{\vec{k}}| = \arccos[\cos(\theta_{\vec{k}}) \cos(\alpha_{\vec{k}})]/T. \quad (21)$$

The details of calculation of the Floquet spectrum is given in Appendix E.

Having obtained an expression for the Floquet spectrum, we now express the elements of $\mathcal{C}_n(l)$ (Eqs. 9 and 8) in terms of parameters of $U_{\vec{k}}$. A straightforward calculation (see Appendix D for details) yields, for $L \to \infty$ and $|\psi(t = 0)\rangle_{\vec{k}} = (0, 1)^T$, where $\delta C_{ij}(n) = \langle c_{\vec{i}}^\dagger c_{\vec{j}}\rangle_n - \langle c_{\vec{i}}^\dagger c_{\vec{j}}\rangle_\infty$ and similarly for $\delta F_{ij}(n)$:

$$\begin{aligned} \delta C_{ij}(n) &= \int \frac{d^d k}{(2\pi)^d} f_1(\vec{k}) \cos(2n\phi_{\vec{k}}) \quad (22) \\ \delta F_{ij}(n) &= \int \frac{d^d k}{(2\pi)^d} (f_2(\vec{k}) \cos(2n\phi_{\vec{k}}) + f_3(\vec{k}) \sin(2n\phi_{\vec{k}})) \end{aligned}$$

with

$$\begin{aligned} f_1(\vec{k}) &= -(1 - \hat{n}_{\vec{k}3}^2) \cos(\vec{k} \cdot (\vec{i} - \vec{j})), \; f_2(\vec{k}) = -i\hat{n}_{\vec{k}3} f_3(\vec{k}) \\ f_3(\vec{k}) &= i(n_{\vec{k}1} + in_{\vec{k}2}) \sin(\vec{k} \cdot (\vec{i} - \vec{j})). \end{aligned} \quad (23)$$

Importantly, $f_{1,2,3}(\vec{k})$ all vanish at the BZ edges and center.

It is clear from Eq. 22 that for large n, the dominant contributions to the relaxation behavior comes from the

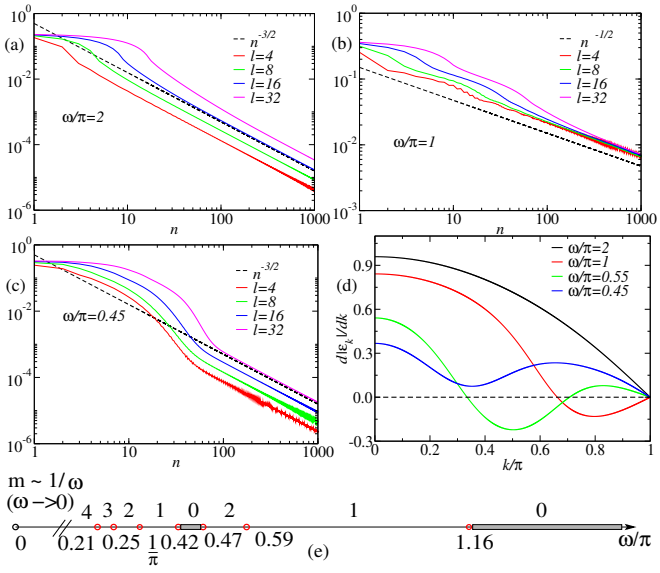

FIG. 4: $\mathcal{D}$ versus n for several l for 1D Ising model and for (a) $\omega = 2\pi$, (b) $\omega = \pi$, and (c) $\omega = 0.45\pi$. (d) Plot of $d|\epsilon_k|/dk$ versus k for several ω. (e) Sketch of the of number of zeroes (m) of $d|\epsilon_k|/dk$ with $k \in (0, \pi)$ as a function of ω showing re-entrant behavior. The thick (thin) regions indicate regimes with $n^{-3/2}(n^{-1/2})$ decay. All parameters are same as in Fig. 1.

stationary points of $\phi_{\vec{k}}$: $d|\vec{\epsilon}_{\vec{k}}|/dk_i = 0$. Using Eq. 21, we find that such stationary points occur if either

$$\cot(\theta_{\vec{k}}) d\alpha_{\vec{k}}/dk_i = -\cot(\alpha_{\vec{k}}) d\theta_{\vec{k}}/dk_i \tag{24}$$

or $\sin(\theta_{\vec{k}}) = 0 = d\alpha_{\vec{k}}/dk_i$. We note that Eq. 24 holds for any protocol; the protocol details appear in the expression of $\theta_{\vec{k}}$ and $\alpha_{\vec{k}}$ without altering its form.

B. Approach to steady state in $d = 1$

For $d = 1$ models, when $\omega \gg 1$, one can approximate $H_{kF} \sim \bar{H}(k)$, where $\bar{H}$ denotes the time-averaged Hamiltonian over one cycle, by using $1/\omega$ as a perturbation parameter in the Dyson series for U_k. In this limit, there are two stationary points at $k = 0, \pi$ and thus $\sin(\theta_{\vec{k}}) = 0 = d\alpha_{\vec{k}}/dk_i$ is satisfied. As ω is decreased below ω_c, an additional stationary point emerges at $k = k_0 \in (0, \pi)$ which satisfies Eq. 24(Fig. 4(d)). This leads to a qualitative change in the relaxation properties of the matrix elements (Eq. 22) which can be understood as follows. The contribution of a saddle point at $k = k_0$ to Eq. 22 can be estimated to be

$$\int f_i(\vec{k}) \exp(in\phi(\vec{k})) d^d k \approx \exp(in\phi(\vec{k}_0))(n|\phi^{''}(\vec{k}_0)|)^{-d/2} \times \exp(\pi i \mu/4) \left(f_i(\vec{k}_0) + i \frac{f_i^{''}(\vec{k}_0)}{2\phi^{''}(\vec{k}_0)} \frac{1}{n} + \mathcal{O}(1/n^2) \right) \tag{25}$$

where μ is the sign of $\phi^{''}(\vec{k}_0)$, and $f_i(\vec{k})$ are smooth functions around $\vec{k} = \vec{k}_0$. For $d = 1$, at $k = 0, \pi$, $\sin(\theta_k) = 0$, *i.e.*, $\hat{n}_{k1}, \hat{n}_{k2} = 0$ and $\hat{n}_{k3} = \pm 1$ leading to $f_i(k_0) = 0$. If these happen to be the only zeroes of $d|\epsilon_k|/dk$, all elements of $\mathcal{C}_n(l)$ (and hence $\mathcal{D}$) receive first non-zero contribution from the $f''(k)$ term in Eq. 25 leading to a convergence to the GGE as $(\omega/n)^{3/2}$. However, for a smaller ω the contribution from stationary point at $k = k_0 \neq 0, \pi$ (where $f_i(k_0) \neq 0$) changes the relaxation behavior of $\mathcal{D}$ to $(\omega/n)^{1/2}$(Eq. 25). The appearance of such a new zero constitute a change in topology of spectrum of H_F. In addition, ω_c is expected to be finite in general since the number of zeroes of $d|\epsilon_k|/dk$ cannot change continuously with ω. In fact, this number cannot change *perturbatively* in $1/\omega$ and hence, the dynamical transitions we discuss here are beyond a Magnus expansion treatment of the Floquet Hamiltonian (for a review of which, see Ref. 26) to any order.

Indeed for the square pulse protocol it can be shown the first zero of $d|\epsilon_k|/dk$ where $k \neq 0, \pi$ appears at a finite ω_c value (details given in Appendix. E) which satisfies

$$(g_i + g_f + 2g_i g_f) T_0 \sin\left((2 + g_i + g_f) T_0\right) + \frac{(g_f - g_i)^2 \sin\left((1 + g_i) T_0\right) \sin\left((1 + g_f) T_0\right)}{(1 + g_i)(1 + g_f)} = 0 \tag{26}$$

where $T_0 = \pi/\omega_c$ is the first non-zero solution of Eq. 26 given g_i and g_f. Hence our result constitutes an example of change in relaxation behavior of *any correlation function* of a periodically driven integrable Hamiltonian due to change of topology of their H_F[46]. We note that the transition unraveled in this work is of fundamentally different origin from dynamical transitions discussed in Refs. 26–29; in contrast to these transitions, the present one leaves its imprint on the temporal behavior of *all* local correlation functions.

As ω is decreased, the number of zeroes of $d|\epsilon_k|/dk$, m, between $0 < k < \pi$ changes. Such a change is non-monotonic in nature for large ω (Fig. 4(c) and (d)) where m is small. It is thus possible that in some frequency range m may revert back to zero leading to re-entrant behavior; numerically, for square pulse protocol, we find

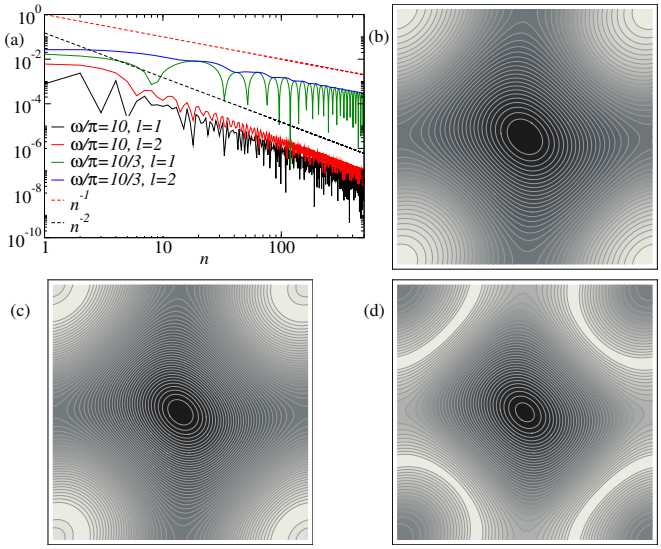

FIG. 5: (a) $\mathcal{D}$ versus n for 2D Kitaev model for $l = 1, 2$ with $J_1 = J_2 = 1$, $g_i = J_3(0) = 5$ and $g_f = J_3(T/2) = 4$. (b), (c), and (d): Contours of $|\vec{\epsilon}_{\vec{k}}|$ versus (k_x, k_y) for $\omega = 10\pi$ (b), 4π (c) and 3.3π (d) indicating a transition at $\omega_c \simeq 4\pi$; white (black) denotes high (low) values.

that this occurs at $\omega_c = 0.47\pi$ for $g_i = 2, g_f = 0$ (Fig. 4(e)). As ω is further decreased, m becomes finite at $\omega = 0.42\pi$ and continue to increase monotonically with decreasing ω: in fact $m \sim \omega^{-1}$ for small ω (Fig. 4(e)) (and this is a generic feature[46]), thus ruling out re-entrance here and leading to a $(\omega/n)^{1/2}$ convergence to steady state as $\omega \to 0$. The phase diagram for the two dynamical regimes has a rich structure as a function of the amplitude and frequency of the periodic drive due to the re-entrance effects and this will be worked out in more detail in Sec. III D.

C. Approach to steady state in $d > 1$

For $d > 1$, we note that for large ω, the condition $\sin(\theta_{\vec{k}}) = 0 = d\alpha_{\vec{k}}/dk_i$ is expected to be satisfied leading to $\mathcal{D} \sim (\omega/n)^{(d+2)/2}$. As ω is decreased, new zeros of $d|\vec{\epsilon}_{\vec{k}}|/dk_i$ are expected to appear at $\vec{k} = \vec{k}_0$ which satisfies Eq. 24. Generically, one expects such solutions to constitute discrete point(s) in the Brillouin zone or there may be no solutions at all. In the former case, one would find a transition to $(\omega/n)^{d/2}$ scaling (Eq. 25) along with possible re-entrant behavior similar to the $d = 1$ model.

However, for a class of 2D models, including the Kitaev model, the existence of a special symmetry leads to solution of Eq. 24 along a line(s) in the Brillouin zone. For the Kitaev model, this can be understood from the fact that the Hamiltonain (for which $b_{\vec{k}} = -[J_1 \cos(k_x) + J_2 \cos(k_y)]$, $\Delta_{\vec{k}} = J_1 \sin(k_x) + J_2 \sin(k_y)$ and $g(t) = J_3(t)$ remain invariant under the simultaneous transformations $J_1 \leftrightarrow J_2$ and $k_x \leftrightarrow k_y$. The dynamics preserves this symmetry; consequently the zeroes of $\partial|\vec{\epsilon}_{\vec{k}}|/\partial k_x$ and $\partial|\vec{\epsilon}_{\vec{k}}|/\partial k_y$ coincide and form a 1D curve in the 2D Brillouin zone leading to a line of zeroes. This phenomenon is illustrated in Fig. 5(b) (c) and (d). The additional line of zeroes appears when ω is changed from 10π (Fig. 5(b)) to 3.3π (Fig. 5(d)). The critical point, where the line of zeroes first appear is $\omega_c \simeq 4\pi$ (Fig. 5(c)). The corresponding plot of $\mathcal{D}$ for $l = 1$ and $l = 2$ as a function of n (Fig. 5(a)) shows two different relaxation behavior in accordance with our analysis. The presence of such line of zeroes excludes the possibility of re-entrant behavior since an entire line of zeroes can not generically vanish at a single ω as it is varied.

To understand the point discussed above in a bit more general setting, let us consider a class of Hamiltonians which has the form

$$\begin{aligned} H_{\vec{k}} &= h[g_1(k_x) + \alpha_1 g_0(k_y), g_2(k_x) + \alpha_2 g_2(k_y)...; \beta(t)] \\ &\equiv h[g_p(k_x) + \alpha_p g_p(k_y); \beta(t)] \end{aligned} \tag{27}$$

for $1 \le p \le p_{\max}$, where g_p are arbitrary functions of k_x or k_y and α_p are parameters of $H_{\vec{k}}$. For example, for the Kitaev model $p_{\max} = 2$, $g_1 = \cos(k_i)$, $g_2 = \sin(k_i)$, $\beta(t) = J_3(t)/J_1$, and $\alpha_1 = \alpha_2 = J_2/J_1$. It is easy to see that the drive does not change this functional form; thus $U_{\vec{k}}$ and hence $H_{\vec{k}F}$ and $|\epsilon_{\vec{k}}|$ retains the same structure

$$|\epsilon_{\vec{k}}| = h'[g_p(k_x) + \alpha_p g_p(k_y); T]. \tag{28}$$

Such a functional form guarantees that if $\partial|\vec{\epsilon}_{\vec{k}}|/\partial k_x = 0$ so is $\partial|\vec{\epsilon}_{\vec{k}}|/\partial k_y$. This implies that the zeroes of $\partial|\vec{\epsilon}_{\vec{k}}|/\partial k_x$ (or equivalently $\partial|\vec{\epsilon}_{\vec{k}}|/\partial k_y$) forms a 1D curve in the 2D Brillouin zone leading to a line of zeroes of $\nabla|\vec{\epsilon}_{\vec{k}}|$. The generalization of this result for $d > 2$ may lead to $d' < d$ hypersurfaces of zeroes of $\nabla|\vec{\epsilon}_{\vec{k}}|$ in a d-dimensional Brillouin zone.

D. Phase diagram for the Ising model

In this section, we sketch the phase diagram for dynamical phases for the 1D transverse field Ising model as a function of the initial transverse field g_i and the drive frequency ω for the square pulse protocol. In what follows, we shall either use this protocol or the periodic kick protocol for which

$$g(t) = g_0 + g_1 \sum_{n=0}^{\infty} \delta(t - nT). \tag{29}$$

where the analysis is simplified further.

Such a phase diagram for the square pulse drive for $g_f = 0$ is shown in Fig. 6 and for $g_f = 2$ in Fig. 7. Note that in the latter case, the equilibrium critical point at $g = 1$ is never crossed during the dynamics. In both cases, we see intermittent regions of $n^{-3/2}$ (grey) and $n^{-1/2}$ (white) relaxation to the final steady state. The relaxation is always $n^{-3/2}$ in the $\omega \to \infty$ limit and $n^{-1/2}$ in the $\omega \to 0$ limit inspite of multiple re-entrances present

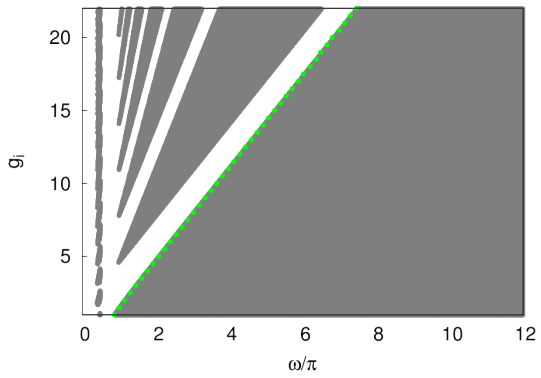

FIG. 6: Phase diagram for the dynamical phases for the square pulse drive protocol where $g_f = 0$. The grey (white) regions correspond to a relaxational behavior of $n^{-3/2}$ ($n^{-1/2}$) of local quantities to their corresponding steady state values. The green dots have been obtained using Eq. 26.

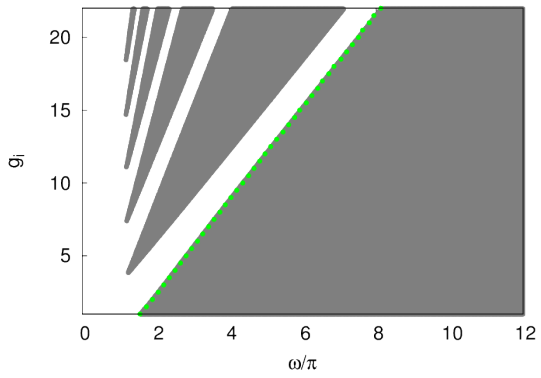

FIG. 7: Phase diagram for the dynamical phases for the square pulse drive protocol where $g_f = 2$. The color scheme is the same as in Fig. 6. The green dots have been obtained using Eq. 26. Note that the equilibrium critical point at $g = 1$ is never crossed during the dynamics here.

in the phase diagram, consistent with the general argument presented in Sec. III B. Furthermore, the number of re-entrant regions increase as the amplitude of the drive g_i is increased in both cases. We also show the perfect match for the location of the first dynamical phase transition as the frequency is reduced at any fixed g_i using Eq. 26 in the phase diagrams presented in Fig. 6 and Fig. 7.

A similar plot for the delta function kicked protocol given by Eq. 29 is shown in Fig. 8. Next, we analyze the phase diagram obtained by using the delta function kick protocol analytically. The evolution operators for this

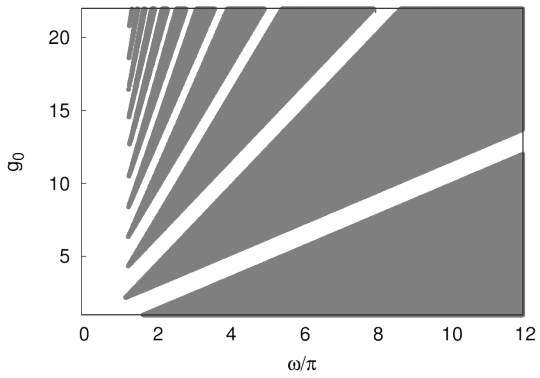

FIG. 8: Phase diagram for the delta function kick protocol where we fix $g_1 = 1$. The color scheme is the same as in Fig. 6 and Fig .7.

protocol is given by

$$\begin{aligned} U_k(T,0) &= e^{-ig_1\tau_3}e^{-iT((g_0-\cos(k))\tau_3+\sin(k)\tau_1)} \\ &= \begin{pmatrix} \alpha_k & -\beta_k^* \\ \beta_k & \alpha_k^* \end{pmatrix} \\ \alpha_k &= e^{-ig_1}(\cos(\Phi_k) - i\sin(\Phi_k)\hat{n}_{kz}) \\ \beta_k &= -ie^{-ig_1}\hat{n}_{kx}\sin(\Phi_k) \end{aligned} \tag{30}$$

where we have $\epsilon_k = \sqrt{(g_0-\cos(k))^2 + (\sin(k))^2}$, $\hat{n}_{kx} = \sin(k)/\epsilon_k$, $\hat{n}_{ky} = 0$, $\hat{n}_{kz} = (g_0 - \cos(k))/\epsilon_k$, and $\Phi_k = T\epsilon_k$. Using Eq. 30, one can find the Floquet spectrum to be

$$\alpha_{kF} = \frac{1}{T}\arccos[\cos(\Phi_k + g_1) + (1-\hat{n}_{kz})\sin(\Phi_k)] \tag{31}$$

For further analysis, we note that $\hat{n}_{kz} \to 1$ for $g_0 \gg 1$ allowing a perturbative expansion of α_{kF}. This leads to

$$\alpha_{kF} = \epsilon_k + \frac{g_1}{T} - \frac{\sin^2 k \sin(\Phi_k)\sin(g_1)}{2T(g_0-\cos(k))^2|\sin(\Phi_k+g_1)|} \tag{32}$$

Having obtained α_{kF}, we now look for zeroes of $d(\alpha_{kF})/dk = 0$. If these occur only at $k = 0, \pi$, the relaxation behavior of the system will demonstrate $n^{-3/2}$ behavior. Thus $n^{-1/2}$ relaxation occurs when the zeroes of $d(\alpha_{kF})/dk$ occurs at other values of k; the condition for this can be shown, after some straightforward algebra, to be

$$\begin{aligned} &\frac{g_0}{\epsilon_k}\left(1 - \frac{\sin^2 g_1 \sin^2 k\ \mathrm{Sgn}(\sin(\Phi_k+g_1))}{2g_0^2\sin^2(\Phi_k+g_1)}\right) \\ &\qquad = \frac{\cos k \sin\Phi_k \sin g_1}{g_0^2 T|\sin(\Phi_k+g_1)|} \end{aligned} \tag{33}$$

where Sgn denotes the signum function. We note that for large g_0, Eq. 33 is satisfied within a small parameter range around the point $(\Phi_k + g_1) = m\pi$ (where $m \in Z$) for which $g_0|\sin(\Phi_k+g_1)| \sim 1$. This implies that the

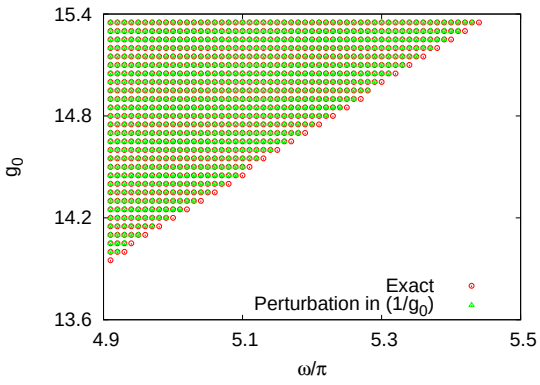

FIG. 9: Phase diagram for the delta function kick protocol where we fix $g_1 = 1.0$ and vary g_0. The white region indicates $n^{-3/2}$ relaxation of local quantities to their final steady state values. The green points denote the perturbative results obtained from solution of Eq. 33 for large g_0 while the red points denotes the exact results for the $n^{-1/2}$ relaxation behavior.

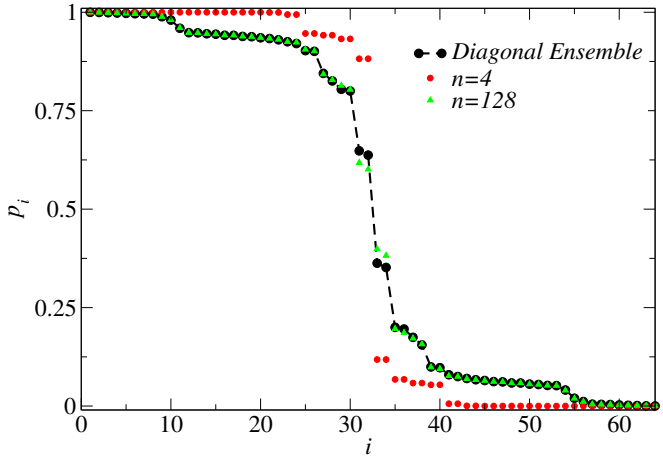

FIG. 10: The approach of the eigenvalues of the correlation matrix of a subsystem of size $l = 32$ to the Diagonal ensemble results as a function of n for the 1D Ising model driven according to a square pulse protocol with $g_i = 3$, $g_f = 2$ and $T = 2$. At small n, the majority of p_i are either 0 or 1.

density of re-entrant regions scale as g_0 at large g_0, which explains the increase in the number of re-entrant regions as the drive amplitude is increased. A computation of the phase diagram with exact numerical result is shown in Fig. 9; we find the perturbative and numerical results match well in the large g_0 regime, and thus $1/g_0$ acts as a suitable expansion parameter unlike $1/\omega$ to get the dynamical transitions.

IV. ENTANGLEMENT IN THE STEADY STATE

In this section, we shall address the entanglement entropy in the final steady state and calculate $S_\infty(l)$. In the $n \to \infty$ limit, the calculation becomes simple since the system can be described locally by the Diagonal ensemble. The computation proceeds in the following manner. Given an initial state at $t = 0$, $|\psi\rangle = \otimes_{\vec{k}} |\psi_{\vec{k}}(t = 0)\rangle$, we can express each $|\psi_{\vec{k}}(t = 0)\rangle$ in terms of the eigenvectors $|1_{\vec{k}}\rangle, |2_{\vec{k}}\rangle$ of the Floquet Hamiltonian $H_{\vec{k}F}$. Then, it follows that

$$\langle\psi_{\vec{k}}(nT)|O_{\vec{k}}|\psi_{\vec{k}}(nT)\rangle = |a_{1\vec{k}}|^2\langle 1_{\vec{k}}|O_{\vec{k}}|1_{\vec{k}}\rangle + |a_{2\vec{k}}|^2\langle 2_{\vec{k}}|O_{\vec{k}}|2_{\vec{k}}\rangle + a^*_{1\vec{k}}a_{2\vec{k}}e^{-i2n|\vec{\epsilon}_{\vec{k}}|T}\langle 1_{\vec{k}}|O_{\vec{k}}|2_{\vec{k}}\rangle + a_{1\vec{k}}a^*_{2\vec{k}}e^{i2n|\vec{\epsilon}_{\vec{k}}|T}\langle 2_{\vec{k}}|O_{\vec{k}}|1_{\vec{k}}\rangle \quad (34)$$

where $a_{1(2)\vec{k}} = \langle 1(2)_{\vec{k}}|\psi_{\vec{k}}(t = 0)\rangle$. It is then justified to drop the rapidly oscillating cross-terms when $n \to \infty$ for calculating the expectation value of any local (in space) operator in the thermodynamic limit. The steps are explicitly shown for the correlation matrix $\mathcal{C}_\infty(l)$ in Appendix D. Dropping the cross-terms in Eq. 34 leads to a mixed density matrix in the orthonormal basis $|1(2)_{\vec{k}}\rangle$ which is called the Diagonal Ensemble and the $n \to \infty$ results for all local quantities and the entanglement entropy of finite subsystems shown here have been obtained from the same.

The entropy of the system in the Diagonal Ensemble, which we denote by $S_{\rm DE}$, may be readily calculated. Dropping the cross-terms from Eq. 34 in the thermodynamic limit, we obtain

$$\frac{S_{\rm DE}}{L^d} = s_{\rm DE} = \frac{2}{(2\pi)^d}\int_{\vec{k}\in BZ/2} d^dk s_{\vec{k}}$$
$$s_{\vec{k}} = -p_{\vec{k}}\log p_{\vec{k}} - (1 - p_{\vec{k}})\log(1 - p_{\vec{k}}) \quad (35)$$

where $p_{\vec{k}} = |a_{1\vec{k}}|^2$ and $s_{\vec{k}}$ is the entropy at momentum $\vec{k}$ (which is a good quantum number here since we look at the entropy of the full system in Eq. 35). $s_{\vec{k}}$ equals zero if $p_{\vec{k}} = 0, 1$ and is maximized to $\ln(2)$ for $p_{\vec{k}} = 1/2$. If the integral $\int_{\vec{k}\in BZ/2} d^dk s_{\vec{k}}$ is finite, then the entropy $S_{\rm DE}$ clearly scales extensively. We see that the eigenvalues of the matrix $\mathcal{C}_n(l)$ approach those of $\mathcal{C}_\infty$ for any $l \ll L$ when n is large enough (Fig. 10). Thus, the entanglement entropy density $S_\infty(l)/l^d$ when $l \to \infty$ and $l/L \to 0$ coincides with $s_{\rm DE}$ (Eq. 35).

The entropy per site $s_{\rm DE}$ shows a non-monotonic behavior as a function of ω. More interestingly, there are sharp features at particular values of ω in $s_{\rm DE}$ (Fig. 11(a)) in $d = 1$. We further show here that these features are in fact derivative singularities that are either cusps or kinks (Fig. 11(b)). The analysis is greatly simplified if the initial state $|\psi_k(t = 0)\rangle$ is taken to be $(0, 1)^T$ at each k. For the 1D Ising model, this corresponds to the ground state at $g \to \infty$. Then, it is straightforward to show that

$$s_k = -\frac{1 - \hat{n}_{k3}}{2}\ln\left(\frac{1 - \hat{n}_{k3}}{2}\right) - \frac{1 + \hat{n}_{k3}}{2}\ln\left(\frac{1 + \hat{n}_{k3}}{2}\right) \quad (36)$$

Thus, $s_k = 0$ if $\hat{n}_{k3} = \pm 1$ and attains its maximum value of $\ln(2)$ when $\hat{n}_{k3} = 0$.

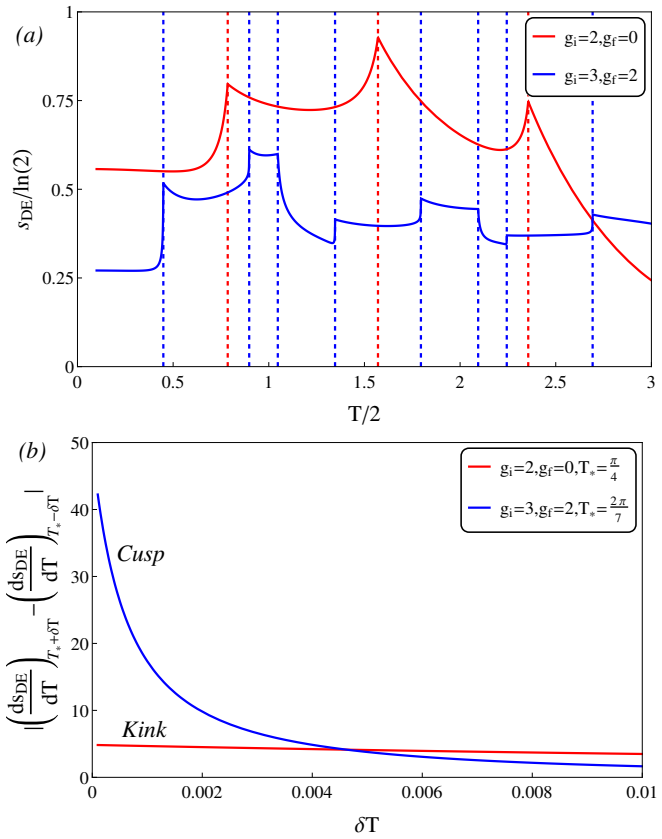

FIG. 11: (a) The entropy per site in the diagonal ensemble $s_{\rm DE}$ as a function of $T = 2\pi/\omega$ for the 1D transverse field Ising model. The initial state is taken to be $\sigma_i^x = 1$ for all i, and the system is then driven using a square pulse protocol with $g_i = 2, g_f = 0$ (red curve) and $g_i = 4, g_f = 2$ (blue curve with $s_{\rm DE}$ multiplied by a factor of two in this case). The locations of the singularities (dashed vertical lines, where red lines are for $g_i = 2, g_f = 0$ and blue lines are for $g_i = 3, g_f = 2$) have been obtained using Eq. 41. (b) Derivative singularities which are either cusps or kinks exist in $s_{\rm DE}$ at the driving time periods T_* where the Floquet bands cross each other.

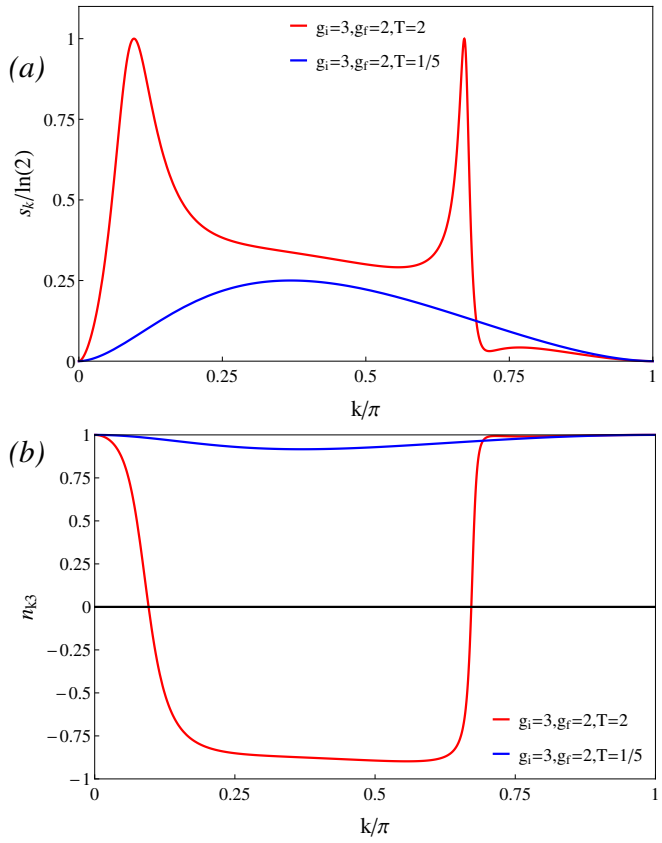

FIG. 12: (a) s_k as a function of k for the square pulse protocol with $g_i = 3$, $g_f = 2$ and drive time period $T = 1/5$ (blue curve) and $T = 2$ (red curve). (b) s_k attains its maximum value of ln(2) whenever $\hat{n}_{k3} = 0$.

In the large ω limit, the Floquet Hamiltonian $\mathcal{H}_{kF}$ can be well approximated by the average Hamiltonian over one cycle and thus $\hat{n}_{k3}$ does not have any zeroes in $k \in [0, \pi]$ except at $k = 0$ or $k = \pi$ in special cases when $g_{\rm av} = (1/T)\int_0^T g(t)dt = \pm 1$. As ω is decreased, new zeroes of $\hat{n}_{k3}$ are generated between the zone boundaries $k = 0$ and $k = \pi$ (Fig. 12(b)) which leads to the presence of newer peaks in the function s_k (Fig. 12(a)). These zeros occur at $k = k_0$ such that

$$\cos(\theta_{k=k_0}) = 0 \quad \text{or} \quad \sin(\alpha_{k=k_0}) = 0. \tag{37}$$

The number of zeroes in the function n_{k3} scales as $1/\omega$ when $\omega \to \infty$. In $d > 1$, the new zeroes in $\hat{n}_{\vec{k}3}$ appear along $(d-1)$-dimensional hypersurfaces in the d-dimensional BZ.

We now consider the total number of zeroes in $\hat{n}_{k3}$ where $k \in (0, \pi)$ (thus excluding $k = 0$ and $k = \pi$). The frequencies $\omega_* = \frac{2\pi}{T_*}$ across which this number changes by one are precisely the locations of the singularities in $s_{\rm DE}$ in 1D (dashed lines marked in Fig. 11(a)). The new zero in $\hat{n}_{k3}$ has to enter/exit from either of the zone boundaries at $k = 0$ or $k = \pi$. However, $\hat{n}_{k3}$ equals ± 1 at the boundaries and hence, the only way a zero can enter/exit is if $\hat{n}_{k3} = \pm 1$ jumps to $-\hat{n}_{k3} = \mp 1$ at the zone boundary from where the new zero enters/exits. Hence, the function $\hat{n}_{k3}$ is necessarily singular at $\omega = \omega_*$ with

$$\left(\frac{d\hat{n}_{k3}}{d\omega}\right)_{\omega\to\omega_*^-,k\to 0/\pi} \neq \left(\frac{d\hat{n}_{k3}}{d\omega}\right)_{\omega\to\omega_*^+,k\to 0/\pi}. \tag{38}$$

The behavior of $\hat{n}_{k3}$ as a function of k is shown in Fig. 13 in the vicinity of one such ω_*. The singularity in $\hat{n}_{k3}$ leads to the resulting derivative singularity in $s_{\rm DE}$ through the relation:

$$\left(\frac{ds_{\rm DE}}{d\omega}\right) = \frac{1}{2}\int_0^\pi dk \log\left(\frac{1-\hat{n}_{k3}}{1+\hat{n}_{k3}}\right)\frac{d\hat{n}_{k3}}{d\omega}, \tag{39}$$

which we show can be either a cusp or a kink singularity in Fig. 11(b).

We now show that these ω_* are located at the frequencies where the Floquet bands $\pm\Phi_k$, defined by $U_k =$

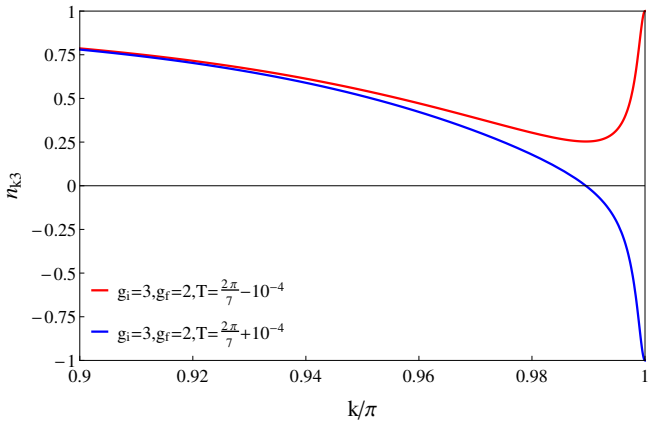

FIG. 13: The behavior of $\hat{n}_{k3}$ when $k \to \pi$ and $T = T_* \pm 10^{-4}$ where $T_* = 2\pi/\omega_*$ corresponds to a Floquet band crossing at $k = \pi$. The drive follows a square pulse protocol with $g_i = 3$ and $g_f = 2$.

$\exp(\pm i\Phi_k)$, cross each other. This is equivalent to the condition that $U_k = \pm I$. For the class of models we consider here (Eq. 3), it was shown in Ref. 48 that such crossings can only occur at those momenta k_0 where $\Delta_{k_0} = 0$, and thus U_{k_0} and $\hat{n}_{k_0 3}$ may be straightforwardly calculated for any protocol. Specializing to 1D, we use Eq. E4 to obtain $\hat{n}_{k3}$ at $k = 0, \pi$ for the square pulse protocol which gives

$$\begin{aligned} \hat{n}_{k=0,3} &= \mathrm{Sgn}\left(\sin(T(g_{\rm av} - 1))\right) \\ \hat{n}_{k=\pi,3} &= \mathrm{Sgn}\left(\sin(T(g_{\rm av} + 1))\right) \end{aligned} \tag{40}$$

Thus, $\hat{n}_{k=0/\pi,3}$ jumps from ± 1 to ∓ 1 whenever

$$\omega_* = \frac{2(g_{\rm av} \pm 1)}{n} \tag{41}$$

where n is any positive integer. This is also precisely the condition to obtain $U_k = \pm I$ at $k = 0/\pi$, and hence the singularities in $s_{\rm DE}$ occur at the Floquet band crossings (as shown in Fig. 11(a)). Since the only details of the drive protocol that enters U_k when $\Delta_{k_0} = 0$ are $g_{\rm av}$, T and k_0, the condition for ω_* (Eq. 41) stays unchanged for any drive protocol in 1D. These arguments can be easily carried over to $d > 1$ and the Floquet band crossings may again lead to singularities in $S_{\rm DE}/L^d$, though such singularities will get weaker (if they survive at all) because of the d-dimensional integrals in $\vec{k}$ space.

V. DISCUSSION

In this work, we have studied entanglement generation and pointed out the presence of a dynamical transition in a class of periodically driven integrable models. Our work shows that the states of such systems crosses over from an area- to volume-law entanglement entropy in a complex manner depending on the drive frequency and the number of drive cycles. This leads to the presence of non-area and non-volume like behavior of $S(l)$: $S(l) \sim l^\alpha$ with $d - 1 \leq \alpha \leq d$; we note that our work shows that states with such non-area and non-volume law entanglement can be generated in a controlled manner by tuning the drive frequency.

We also study the relaxation behavior of the correlation function and the density matrices of such periodically driven systems to their steady state (GGE) values as a function of the number of drive frequency. In doing so, we unravel a frequency controlled dynamic transition between two phases of the system. In the high frequency regime, S_n decays to S_∞ as $n^{-d/2-1}$ while below a critical frequency, it does so as $n^{-d/2}$. We show that this transition can be understood as a change in topology of the Flouqet spectrum and leads to change in behavior of local correlation function. This is in sharp contrast to other class of dynamic transition studied in the literature[26–29] which is associated with non-analyticities (also known as Fischer zeroes) of the dynamical free energy of the system $f(z) = -\lim_{L\to\infty} \ln(F(z))/L^d$, where z is obtained by analytic continuation of time t in the complex plane and which do not leave their mark on local correlation function. We present a detailed phase diagram corresponding to these transition and provide an analytical expression for one of the phase boundaries for the square pulse protocol which matches exact numerics. We also show that a perturbative expansion in terms of the inverse of the drive amplitude captures the dynamical transitions reliably in the large amplitude limit, whereas an expansion in $1/\omega$ fails to do so.

Finally, we also study the entanglement entropy of such driven systems in the steady state described by the diagonal ensemble. We find that in 1D S_∞/L displays singular cusp/kink like features as a function of ω at special values of the drive frequencies: $\omega = \omega^*$. We identify the presence of such cusp/kink like features with Floquet band crossings and provide an explicit expression of ω^* for arbitrary drive protocol. We note that for a large number of drive protocols such Floquet band crossings indicate topological transitions of driven systems; thus our results indicate that the steady state entanglement entropy bears signatures of such topological transitions. We also note that our arguments in this regard may be carried over to integrable systems with $d > 1$. However, it is not clear whether such singular features in S_∞/L^d will survive due to effect of higher dimensional momentum integrals involved in computation of S_∞/L^d.

We note that our work can be verified using simple experiments. Recently second Rényi entropy $S^{(2)} = -\mathrm{Tr}[\rho^2]$ has been measured via measurement of overlap of two quantum many-body states of ultracold atom systems[49]. We propose analogous measurement of $S_n^{(2)}$ (which has similar properties as S_n) as function of n and predict its $(\omega/n)^{(d+2)/2}[(\omega/n)^{d/2}]$ scaling for fast [slow] drives. The different dynamical regimes and their reentrant behavior may also be experimentally observed via magnetization ($\langle\sigma_x\rangle_n$) measurement of the periodically

driven Ising model. We note here that such ultracold atom setups are currently experimentally feasible[22,50].

In conclusion, we have demonstrated controlled realization of quantum states with non-area and non-volume law entanglement entropy and predicted the presence of two distinct dynamical phases separated by transitions arising from change in topology of the system's Floquet spectrum. We have also demonstrated that the steady state entanglement entropy, for 1D integrable systems, displays singular features at special frequencies which is associated with Floquet band crossings. We have suggested specific experiments which can test our theory.

Finally, our work leads to several possibilities of future extensions such as study of possible realization of such dynamical phases in non-integrable and models with long-range interactions.

Appendix A: Ising and Kitaev model

In this section, we sketch the connection of Eq. 3 in the main text with a large class of spin models. For example in $d = 1$, the transverse field Ising model has the Hamiltonian

$$H_{\rm Ising} = -\sum_{j=1}^{N}(h\sigma_j^x + \sigma_j^z\sigma_{j+1}^z), \tag{A1}$$

where $\sigma^{x,y,z}$ are the usual Pauli operators, h denotes the transverse field, and we have scaled all quantities by the nearest neighbor interaction J. The ground state of this model is ferromagnetic when $-1 < h < 1$ and paramagnetic otherwise. There are thus two critical points in this model at $h = \pm 1$. It turns out that $H_{\rm Ising}$ allows a fermionic representation in terms of H with $b_k = \cos(k)$, $\Delta_k = \sin(k)$, $g = h$, and $\psi_k = (c_k, c_{-k}^\dagger)^T$ via a Jordan-Wigner representation given by

$$\begin{aligned}\sigma_n^x &= 1 - 2c_n^\dagger c_n \\ \sigma_n^z &= -(c_n + c_n^\dagger)\prod_{m<n}(1 - 2c_m^\dagger c_m),\end{aligned} \tag{A2}$$

where c_n is the Fermionic annihilation operator on site n and c_k denotes its Fourier transform[36]. This fermionic representation of $H_{\rm Ising}$ has been used, with $g(t)$ following a square pulse protocol, to generate the results shown in Fig. 1, Fig. 2, Fig. 3 and Fig. 4 in the main text.

A similar correspondence can be obtained in $d = 2$ by considering the Kitaev model[19,37,38,40] whose Hamiltonian is given by

$$\begin{aligned}H_{\rm 2D} = \sum_{j+l=\text{even}} (& J_1\sigma_{j,l}^x\sigma_{j+1,l}^x + J_2\sigma_{j-1,l}^y\sigma_{j,l}^y \\ & + J_3\sigma_{j,l}^z\sigma_{j,l+1}^z).\end{aligned} \tag{A3}$$

This Hamiltonian describes a spin model on a hexagonal 2D lattice, where j and l denote the column and row indices of the brick-wall lattice which is an alternative representation of the hexagonal lattice (Fig. 14). The Kitaev

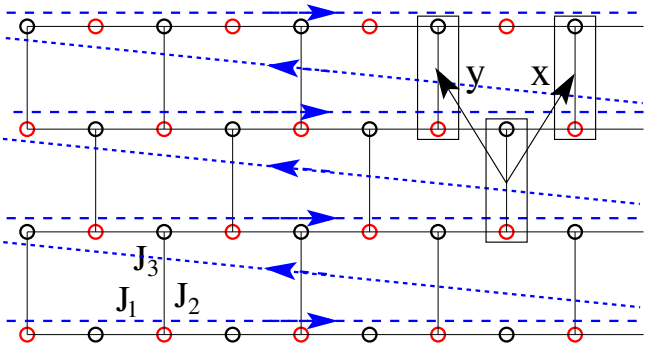

FIG. 14: Brick-wall lattice which is equivalent to the 2D hexagonal lattice and the three types of interactions in the Kitaev model. Also shown is the contour for the Jordan-Wigner transformation that is employed for the fermionization of the model.

model can be fermionized in an analogous manner to the Ising model by taking a Jordan-Wigner transformation along a one-dimensional contour that threads the entire lattice and passes through each lattice site exactly once (Fig. 14). Introducing a pair of Majorana fermions for each fermion, the Kitaev model then reduces to a model of Majorana fermions coupled to Z_2 gauge fields. The crucial point that makes the solution of Kitaev model feasible is that the Z_2 fields, which we denote by α_r, commute with $H_{\rm 2D}$, so that all the eigenstates of $H_{\rm 2D}$ can be labeled by their specific values ($\alpha_r = \pm 1$). It has been shown that for any value of the parameters J_i, the ground state of the model always corresponds to all α_r equal to 1. Since α_r is a constant of motion, the dynamics of the model starting from any ground state never takes the system outside the manifold of states with $\alpha_r = 1$. The Majorana fermions can then be combined pairwise on each J_3 bond (as shown in Fig. 14) to give an equivalent free fermion Hamiltonion on the square lattice[40]:

$$\begin{aligned}H_{2D} &= J_1\sum_r(c_r^\dagger + c_r)(c_{r+\hat{x}}^\dagger - c_{r+\hat{x}}) \\ &+ J_2\sum_r(c_r^\dagger + c_r)(c_{r+\hat{y}}^\dagger - c_{r+\hat{y}}) \\ &+ J_3\sum_r\alpha_r(2c_r^\dagger c_r - 1)\end{aligned} \tag{A4}$$

where $\alpha_r = 1$ if the initial state is a ground state. Thus, like in the 1D case, $H_{\rm 2D}$ allows a fermionic representation in terms of H with $b_{\vec{k}} = J_1\cos(k_x) + J_2\cos(k_y)$, $\Delta_{\vec{k}} = J_1\sin(k_x) + J_2\sin(k_y)$, $g = J_3$, and $\psi_{\vec{k}} = (c_{\vec{k}}, c_{-\vec{k}}^\dagger)^T$. Note that the static Z_2 gauge fields give an additional additive contribution to the entanglement entropy that follows the area law[39] and does not change under the dynamics, whereby we can ignore this (static) contribution while considering the generation of entanglement in a periodic drive.

The energy spectrum of $H_{\rm 2D}$ consists of two bands with

energies

$$E^{\pm}_{\vec{k}} = \pm 2\,[(J_1\sin(k_x)+J_2\sin(k_y))^2 + (J_3 - J_1\cos(k_x)+J_2\cos(k_y)^2]^{1/2}. \quad \text{(A5)}$$

We note for $|J_1 - J_2| \leq J_3 \leq (J_1 + J_2)$, these bands touch each other so that the energy gap $E^+_{\vec{k}} - E^-_{\vec{k}}$ vanishes for special values of $\vec{k}$ leading to the gapless phase of the model. This fermionic representation of H_{2D} has been used, with $g(t)$ following a square pulse protocol, to generate the results shown in Fig. 5 in the main text.

Before ending this section, we note that it is possible to obtain an analytic solution for $|\psi_k(nT)\rangle$ for the square pulse protocol as follows. Within each cycle, for a given g_i, g_f and T, one constructs a unitary matrix matrices $U(\vec{k}, g_i, g_f)$ which evolve an arbitrary initial $|\psi_k(0)\rangle$ to the state after time T by

$$|\psi_{\vec{k}}(T)\rangle = U(\vec{k}, g_i, g_f)|\psi_{\vec{k}}(0)\rangle \quad \text{(A6)}$$

Thus, after n cycles, we get

$$|\psi_{\vec{k}}(nT)\rangle = U^n(\vec{k}, g_i, g_f)|\psi_{\vec{k}}(0)\rangle. \quad \text{(A7)}$$

For the square pulse case, it is easy to see that

$$U(\vec{k}, g_i, g_f) = \exp\left(-iH_{\vec{k}}(g_f)\frac{T}{2}\right)\exp\left(-iH_{\vec{k}}(g_i)\frac{T}{2}\right) \quad \text{(A8)}$$

where $H_{\vec{k}}(g) = (g - b_{\vec{k}})\tau_3 + \Delta_{\vec{k}}\tau_1$ as given in Eq. 3 in the main text.

Appendix B: Protocol independence

We have used the square pulse protocol and the periodic kick protocol for the numerical calculations shown in the main text, mainly due to their simple analytic forms. However, most of our results are protocol independent and we illustrate that here with some results using both the linear ramp and sinusoidal protocols, which we will define below. For notational simplicity, we restrict ourselves to the 1D Ising model.

In the linear ramp protocol with a time period $T = 2T_0$, the precise variation of $g(t)$ between n and $n-1$ cycles is given by

$$\begin{aligned} g(t) &= g_i + (g_f - g_i)(t - 2(n-1)T_0)/T_0, \\ &\quad \text{for} \quad 2(n-1)T_0 \leq t \leq (2n-1)T_0 \\ &= g_f - (g_f - g_i)(t - (2n-1)T_0)/T_0 \\ &\quad \text{for} \quad (2n-1)T_0 \leq t \leq 2nT_0 \end{aligned} \quad \text{(B1)}$$

The advantage of this protocol is that one can again obtain exact analytical solution for the wavefunction at the end of a drive cycle like the square pulse case, though the solution is more complicated. The unitary matrix for the evolution of the wavefunction at the end of one drive can be written as

$$U_k(g_i, g_f) = U_b(k, g_f \to g_i, T_0)U_f(k, g_i \to g_f, T_0) \quad \text{(B2)}$$

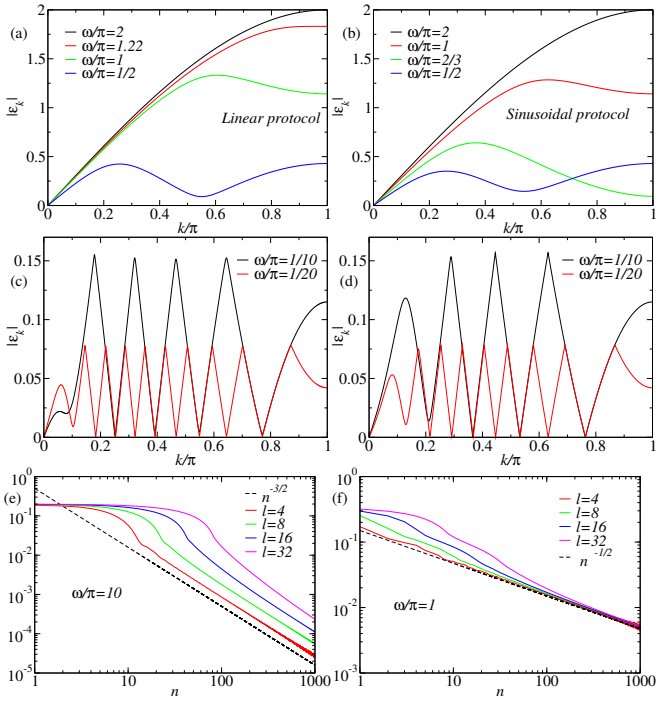

FIG. 15: Panels (a),(b) show the behavior of $|\epsilon(k)|$ as a function of k for a few representative values of ω both for the linear ramp and the sinusoidal drive protocols. Panels (c),(d) show $|\epsilon(k)|$ as a function of k for small values of ω for the linear ramp and the sinusoidal drive protocols, respectively. Panels (e),(f) show the power law decay of $\mathcal{D}$ as a function of n for several l for the linear ramp protocol.

where U_f (U_b) refer to the corresponding unitary matrix for the "forward" ("backward") ramp from g_i to g_f (g_f to g_i). Below, we give the explicit expressions for the two unitary matrices assuming that $g_i > g_f$ without loss of generality (for details, we refer the reader to Ref. 51). The matrices can be more easily expressed through the redefined variables $v = (g_i - g_f)/T_0, T_i = (b_k - g_i)/\sqrt{v}, T_f = \sqrt{v}T_0 - T_i$ and $\omega = \Delta_k/\sqrt{v}$.

Then, for the forward ramp, we have

$$\begin{aligned} (U_f)_{11} &= (U_f)^*_{22} \\ &= \frac{\Gamma(1 - i\omega^2/2)}{\sqrt{2\pi}}[D_{i\omega^2/2}(T_f\sqrt{2}e^{-i\pi/4}) \\ &\times D_{-1+i\omega^2/2}(T_i\sqrt{2}e^{i3\pi/4}) \\ &+ D_{i\omega^2/2}(T_f\sqrt{2}e^{i3\pi/4}) \\ &\times D_{-1+i\omega^2/2}(T_i\sqrt{2}e^{-i\pi/4})], \\ (U_f)_{12} &= -(U_f)^*_{21} \\ &= \frac{\Gamma(1 - i\omega^2/2)}{\omega\sqrt{\pi}}e^{i\pi/4}[-D_{i\omega^2/2}(T_f\sqrt{2}e^{-i\pi/4}) \\ &\times D_{i\omega^2/2}(T_i\sqrt{2}e^{i3\pi/4}) \\ &+ D_{i\omega^2/2}(T_f\sqrt{2}e^{i3\pi/4})D_{i\omega^2/2}(T_i\sqrt{2}e^{-i\pi/4})]. \end{aligned} \quad \text{(B3)}$$

where D denotes the parabolic cylinder function and Γ denotes the gamma function. The unitary matrix for the backward ramp is then obtained from the above matrix using $(U_b)_{ij} = (-1)^{i+j}(U_f^*)_{ij}$.

For the sinusoidal protocol with a time period of T, the variation of $g(t)$ is chosen as follows

$$g(t) = g_{\rm av} + A\cos\left(\frac{2\pi t}{T}\right) \tag{B4}$$

Here, the unitary matrix for one drive cycle cannot be expressed analytically and one has to resort to a numerical solution of the time-dependent Schrödinger equation.

In Fig. 15, we show the results for the linear ramp protocol with $g_i = 2$, $g_f = 0$ and varying $\omega = 2\pi/T$ and for the sinusoidal protocol with $g_{\rm av} = 1$, $A = 1$ and varying $\omega = 2\pi/T$. From Fig. 15(a),(b), it is clear that m, the number of zeroes in $d|\epsilon_k|/dk$ for $0 < k < \pi$ or equivalently the number of local extrema in $|\epsilon_k|$ for $0 < k < \pi$, is zero when $\omega \gg 1$ and attains a non-zero value only below a critical (protocol dependent) ω_c exactly like in the square pulse case. From Fig. 15(c),(d), it is also clear that $m \sim 1/\omega$ for small ω for both the linear ramp and sinusoidal protocols, again like in the case of the square pulse protocol. Lastly, in Fig. 15(e),(f), we show the calculation for the power law decay of $\mathcal{D}$ for two different ω on either side of ω_c for the linear ramp protocol.

These calculations substantiate the protocol independence of our results asserted in the main text.

Appendix C: Computation of $S_n(l)$

As shown in the main text, the state generated after n drive cycles, $|\psi(nT)\rangle$ is the ground state of $\mathcal{H}_t$ (Eq. 11 of the main text) which is quadratic in the fermionic operators c and $c^\dagger$. For such free fermion Hamiltonians, the reduced density matrix for the "ground state" $|\psi(nT)\rangle$ can be written as

$$\rho_\alpha \;=\; \exp(-\mathcal{H}_\alpha)/Z \quad , \mathcal{H}_\alpha = \sum_{i=1}^{l} \epsilon_i \eta_i^\dagger \eta_i \tag{C1}$$

where l is the number of sites in the subsystem denoted by α and the operators $\eta_i, \eta_i^\dagger$ are fermionic operators for single particle states with energies ϵ_i. The constant Z ensures the correct normalization $tr(\rho_\alpha) = 1$. Since *all* correlation functions of the subsystem can be expressed in terms of the quadratic correlations by using Wick's theorem, the entanglement Hamiltonian $\mathcal{H}_\alpha$ (and hence $S(l)$) is determined by the condition that it gives the *right* quadratic correlation functions C_{ij} and F_{ij} for the sites that belong to the subsystem.

Let us denote the Bogoluibov transformation that gives the diagonal representation $\eta, \eta^\dagger$ from $c, c^\dagger$ for the subsystem as

$$\begin{aligned} \eta_k &= \sum_i (g_{ki} c_i + h_{ki} c_i^\dagger) \\ \eta_k^\dagger &= \sum_i (g_{ki}^* c_i^\dagger + h_{ki}^* c_i) \end{aligned} \tag{C2}$$

where i belongs to the sites in the subsystem being considered. Since $\eta, \eta^\dagger$ satisfy anti commutation algebra, we can easily verify that the matrix $\mathbf{T}$ defined as

$$\begin{pmatrix} \mathbf{g} & \mathbf{h} \\ \mathbf{h}^* & \mathbf{g}^* \end{pmatrix} \tag{C3}$$

is a $2l \times 2l$ unitary matrix. Introducing the bra–ket notation,

$$|\phi\rangle = \begin{pmatrix} c \\ c^\dagger \end{pmatrix} \tag{C4}$$

and

$$|\psi\rangle = \begin{pmatrix} \eta \\ \eta^\dagger \end{pmatrix} \tag{C5}$$

The transformation in Eq. C2 is then simply expressed as

$$|\psi\rangle = \mathbf{T}|\phi\rangle \tag{C6}$$

Expressing the entanglement Hamiltonian $\mathcal{H}_\alpha$ as $\phi^\dagger \mathbf{M} \phi$, we see that

$$\mathbf{M} = \mathbf{T}^\dagger \begin{pmatrix} \epsilon & 0 \\ 0 & -\epsilon \end{pmatrix} \mathbf{T} \tag{C7}$$

where the middle matrix is diagonal. Now, calculating the outer product of $|\phi\rangle$ with itself, which we denote by the $2l \times 2l$ matrix $\mathcal{C}$ and which requires the knowledge of two $l \times l$ matrices $\mathbf{C}$ and $\mathbf{F}$, we get

$$\begin{aligned} \mathcal{C} = \langle|\phi\rangle\langle\phi|\rangle &= \mathbf{T}^\dagger \langle|\psi\rangle\langle\psi|\rangle \mathbf{T} \\ \mathbf{T}^\dagger \begin{pmatrix} \frac{1}{\exp(-\epsilon)+1} & 0 \\ 0 & \frac{1}{\exp(\epsilon)+1} \end{pmatrix} \mathbf{T} \end{aligned} \tag{C8}$$

where the middle matrix is again diagonal and we have used $\langle \eta_k^\dagger \eta_{k'} \rangle = \frac{1}{\exp(\epsilon_k)+1}\delta_{k,k'}$. The eigenvalues of $\mathcal{C}$ always come in pairs $p_k, 1-p_k$ where p_k is the probability of occupation of the k^{th} fermionic modes. Then the entanglement entropy $S(l)$ is simply $-\sum_{i=1}^{2l} p_i \log(p_i)$. This result has been used in numerical calculations of the main text.

Appendix D: Details of calculation of $\mathcal{D}$

In this section, we study the relaxation of the system for finite but large n to its diagonal ensemble (equivalently GGE) value discussed in the past section. To

this end, we define a distance measure which provides us information regarding this relaxation as a function of n. For the class of integrable models we consider here, the entanglement properties are solely determined by the two-point correlations of the subsystem as shown in the past section. Thus we define the distance measure using the correlation matrices $\mathcal{C}_\infty(l)$ and $\mathcal{C}_n(l)$. This can be done by using the standard trace distance between these two matrices[45]:

$$D(\mathcal{C}_n(l),\mathcal{C}_\infty(l)) = \frac{1}{2l}Tr\sqrt{(\mathcal{C}_\infty(l)-\mathcal{C}_n(l))^\dagger(\mathcal{C}_\infty(l)-\mathcal{C}_n(l))} \tag{D1}$$

We note that D is positive, lies in $\in [0,1]$, and equals zero only when the two matrices are identical. The matrix elements of $\mathcal{C}_n(l)$ are determined by $\langle c_{\vec{i}}^\dagger c_{\vec{j}}\rangle$ and $\langle c_{\vec{i}}^\dagger c_{\vec{j}}^\dagger\rangle$; so we first calculate how these quantities behave as a function of n when $n \gg 1$. Using Eq. E3, we find, after a few lines of algebra, that in the thermodynamic limit ($L\to\infty$),

$$\begin{aligned}
\langle c_{\vec{i}}^\dagger c_{\vec{j}}\rangle &= \frac{2}{(2\pi)^d}\int_{\vec{k}\in BZ/2} d^dk\ \cos(\vec{k}\cdot(\vec{i}-\vec{j}))\left(\frac{u_{0\vec{k}}^2}{2}(1+\hat{n}_{\vec{k}3}^2)+\frac{v_{0\vec{k}}^2}{2}(1-\hat{n}_{\vec{k}3}^2)+u_{0\vec{k}}v_{0\vec{k}}\hat{n}_{\vec{k}1}\hat{n}_{\vec{k}3}\right)\to \text{GGE}\\
&+ \frac{2}{(2\pi)^d}\int_{\vec{k}\in BZ/2} d^dk\cos(\vec{k}\cdot(\vec{i}-\vec{j}))\left(\left(\frac{u_{0\vec{k}}^2}{2}-\frac{v_{0\vec{k}}^2}{2}\right)(1-\hat{n}_{\vec{k}3}^2)-u_{0\vec{k}}v_{0\vec{k}}\hat{n}_{\vec{k}1}\hat{n}_{\vec{k}3}\right)\cos(2n\phi_{\vec{k}})\\
&- \frac{2}{(2\pi)^d}\int_{\vec{k}\in BZ/2} d^dk\cos(\vec{k}\cdot(\vec{i}-\vec{j}))u_{0\vec{k}}v_{0\vec{k}}\hat{n}_{\vec{k}2}\sin(2n\phi_{\vec{k}})\\
\langle c_{\vec{i}}^\dagger c_{\vec{j}}^\dagger\rangle &= \frac{2}{(2\pi)^d}\int_{\vec{k}\in BZ/2} d^dk\sin(\vec{k}\cdot(\vec{i}-\vec{j}))\left(u_{0\vec{k}}v_{0\vec{k}}\hat{n}_{\vec{k}1}(\hat{n}_{\vec{k}1}+i\hat{n}_{\vec{k}2})+\frac{(u_{0\vec{k}}^2-v_{0\vec{k}}^2)\hat{n}_{\vec{k}3}(\hat{n}_{\vec{k}1}+i\hat{n}_{\vec{k}2})}{2}\right)\to \text{GGE}\\
&+ \frac{2}{(2\pi)^d}\int_{\vec{k}\in BZ/2} d^dk\sin(\vec{k}\cdot(\vec{i}-\vec{j}))\left(u_{0\vec{k}}v_{0\vec{k}}(1-\hat{n}_{\vec{k}1}^2-i\hat{n}_{\vec{k}1}\hat{n}_{\vec{k}2})-\frac{(u_{0\vec{k}}^2-v_{0\vec{k}}^2)\hat{n}_{\vec{k}3}(\hat{n}_{\vec{k}1}+i\hat{n}_{\vec{k}2})}{2}\right)\cos(2n\phi_{\vec{k}})\\
&+ \frac{2}{(2\pi)^d}\int_{\vec{k}\in BZ/2} d^dk\sin(\vec{k}\cdot(\vec{i}-\vec{j}))\left(iu_{0\vec{k}}v_{0\vec{k}}\hat{n}_{\vec{k}3}-i\frac{(u_{0\vec{k}}^2-v_{0\vec{k}}^2)(\hat{n}_{\vec{k}1}+i\hat{n}_{\vec{k}2})}{2}\right)\sin(2n\phi_{\vec{k}})
\end{aligned} \tag{D2}$$

where the integral is taken over half the Brillouin zone (BZ) since the $(\vec{k},-\vec{k})$ fermions are always excited in pairs. It is clear from Eq. D2 that only the terms indicated by GGE survive in the $n\to\infty$ limit. These have been represented as $\langle c_i^\dagger c_j\rangle_\infty$ and $\langle c_i c_j\rangle_\infty$ in the main text. The other terms lead to Eq. 23 of the main text for $u_{\vec{k}}^i \equiv u_{\vec{k}0}=0$ and $v_{\vec{k}i}\equiv v_{\vec{k}0}=1$.

Before ending this section, we note that for large ω in general the condition $\sin(\theta_{\vec{k}})=0=d\alpha_{\vec{k}}/dk_i$ is expected to be satisfied at the minima of $H_{\vec{k}}$. If these minima happen to be at the zone boundary, where $\sin(\vec{k}\cdot(\vec{i}-\vec{j}))$ vanishes, then $f(\vec{k})=0$ (where $f(\vec{k})$ can be read off from Eq. D2), and hence the relaxation of S to GGE will scale as $(\omega/n)^{(d+2)/2}$. However, if the minima of $H_{\vec{k}}$ occurs at $\vec{k}=\vec{k}_1$ so that $\sin(\vec{k}_1\cdot(\vec{i}-\vec{j}))\neq 0$, then $f(\vec{k}_1)\neq 0$ for $\langle c_{\vec{i}}^\dagger c_{\vec{j}}^\dagger\rangle$ and hence S does not scale as $(\omega/n)^{(d+2)/2}$. We note however, that even in this case, all local quantities (such as fermion density which corresponds to magnetization in the spin language) and those which depend only on diagonal correlation functions $\langle c_i^\dagger c_j\rangle$ still exhibits $(\omega/n)^{(d+2)/2}$ scaling and will show the two dynamical regimes discussed in the main text.

Appendix E: Construction of H_F

Let us consider an arbitrary periodic protocol characterized by the number of cycles n and the drive frequency $\omega=2\pi/T$ which takes the system from an initial state $\psi^i=\prod_{\vec{k}}\psi_{\vec{k}}^i=\prod_{\vec{k}}(u_{\vec{k}}^i,v_{\vec{k}}^i)^T$ to a final state $\psi^f=\prod_{\vec{k}}\psi_{\vec{k}}^f=\prod_{\vec{k}}(u_{\vec{k}}^{nf},v_{\vec{k}}^{nf})^T$. In what follows we shall define the state reached after one drive cycle to be $\psi'=\prod_{\vec{k}}\psi'_{\vec{k}}=\prod_{\vec{k}}(u_{\vec{k}}^f,v_{\vec{k}}^f)^T$. One can relate the wavefunctions $\psi'_{\vec{k}}$ and $\psi_{\vec{k}}^i$ through a evolution operator $U_{\vec{k}}$ given by

$$\begin{aligned}
\psi_{\vec{k}}^f &= U_{\vec{k}}^n\psi_{\vec{k}}^i,\quad \psi'_{\vec{k}}=U_{\vec{k}}\psi_{\vec{k}}^i,\\
U_{\vec{k}} &= \begin{pmatrix}\cos(\theta_{\vec{k}})e^{i\alpha_{\vec{k}}} & \sin(\theta_{\vec{k}})e^{i\gamma_{\vec{k}}}\\ -\sin(\theta_{\vec{k}})e^{-i\gamma_{\vec{k}}} & \cos(\theta_{\vec{k}})e^{-i\alpha_{\vec{k}}}\end{pmatrix}=e^{-iH_{\vec{k}F}T}
\end{aligned} \tag{E1}$$

The parametrization of $U_{\vec{k}}$ follows from unitary nature of the evolution and $\theta_{\vec{k}}$, $\alpha_{\vec{k}}$ and $\gamma_{\vec{k}}$ are real-valued functions

of $\vec{k}$. Here H_F is the Floquet Hamiltonian which can be used to describe the state of the system after a drive period; note that the final state after n periods is simply described by $\exp[-inH_{\vec{k}F}T]$.

To make further progress, we express U in terms of $\psi^i_{\vec{k}}$ and $\psi'_{\vec{k}}$. A few lines of straightforward algebra yields

$$\begin{aligned}
\sin^2(\theta_{\vec{k}}) &= \Big[|u^f_{\vec{k}}|^2 v^{i2}_{\vec{k}} + |v^f_{\vec{k}}|^2 u^{i2}_{\vec{k}} \\
&\quad -2|u^f_{\vec{k}}||v^f_{\vec{k}}|u^i_{\vec{k}}v^i_{\vec{k}}\cos(\mu_{\vec{k}}-\mu'_{\vec{k}})\Big] \qquad \text{(E2)}\\
\gamma_{\vec{k}} &= \arctan\left(\frac{|u^f_{\vec{k}}|v^i_{\vec{k}}\sin(\mu_{\vec{k}}) + u^i_{\vec{k}}|v^f_{\vec{k}}|\sin(\mu'_{\vec{k}})}{|u^f_{\vec{k}}|v^i_{\vec{k}}\cos(\mu_{\vec{k}}) - u^i_{\vec{k}}|v^f_{\vec{k}}|\cos(\mu'_{\vec{k}})}\right)\\
\alpha_{\vec{k}} &= \arctan\left(\frac{|u^f_{\vec{k}}|u^i_{\vec{k}}\sin(\mu_{\vec{k}}) - v^i_{\vec{k}}|v^f_{\vec{k}}|\sin(\mu'_{\vec{k}})}{|u^f_{\vec{k}}|u^i_{\vec{k}}\cos(\mu_{\vec{k}}) + |v^f_{\vec{k}}|v^i_{\vec{k}}\cos(\mu'_{\vec{k}})}\right)
\end{aligned}$$

where we have taken $u^i_{\vec{k}}$ and $v^i_{\vec{k}}$ to be real and have parameterized $u^f_{\vec{k}} = |u^f_{\vec{k}}|\exp[i\mu_{\vec{k}}]$ and $v^f_{\vec{k}} = |v^f_{\vec{k}}|\exp[i\mu'_{\vec{k}}]$. We note that $U_{\vec{k}}$ reduces to the identity matrix for $u^f_{\vec{k}} = u^i_{\vec{k}}$ and $v^f_{\vec{k}} = v^i_{\vec{k}}$. Note that for $u^i_{\vec{k}} = 0$ and $v^i_{\vec{k}} = 1$, Eq. E2 reduces to the expressions used in the main text.

Next, we obtain an expression for $H_{\vec{k}F}$. To do this, we note that in the present case $H_{\vec{k}F}$ can be written in the form of a 2×2 matrix which can be expressed in terms of Pauli matrices: $H_{\vec{k}F} = \vec{\sigma}\cdot\vec{\epsilon}_{\vec{k}}$. where $\vec{\epsilon}_{\vec{k}} = (\epsilon_{1k}, \epsilon_{2k}, \epsilon_{3k})$. This allows us to write

$$U_{\vec{k}} = e^{-i(\vec{\sigma}\cdot\vec{n}_{\vec{k}})\phi_{\vec{k}}}, \quad n_{\vec{k}} = \frac{\vec{\epsilon}_{\vec{k}}}{|\vec{\epsilon}_{\vec{k}}|} \quad , \phi_{\vec{k}} = T|\vec{\epsilon}_{\vec{k}}| \quad \text{(E3)}$$

Using Eqs. E1, E2, and E3, one obtains, after some straightforward algebra,

$$\begin{aligned}
n_{\vec{k}1} &= -\sin(\theta_{\vec{k}})\sin(\gamma_{\vec{k}})\sin(\phi_{\vec{k}})/D_{\vec{k}}\\
n_{\vec{k}2} &= -\sin(\theta_{\vec{k}})\cos(\gamma_{\vec{k}})\sin(\phi_{\vec{k}})/D_{\vec{k}}\\
n_{\vec{k}3} &= -\cos(\theta_{\vec{k}})\sin(\alpha_{\vec{k}})\sin(\phi_{\vec{k}})/D_{\vec{k}}\\
D_{\vec{k}} &= \sqrt{1-\cos^2(\theta_{\vec{k}})\cos^2(\alpha_{\vec{k}})}\\
|\vec{\epsilon}_{\vec{k}}| &= \arccos[\cos(\theta_{\vec{k}})\cos(\alpha_{\vec{k}})]/T. \qquad \text{(E4)}
\end{aligned}$$

The last of these expressions is Eq. 21 of the main text. At the edge of the Brillouin zone, where the off-diagonal component of H_k disappears, U_k becomes a diagonal matrix, which in turns makes $\sin(\theta_{\vec{k}}) = 0$. This leads us to the result $n_{\vec{k}1} = n_{\vec{k}2} = 0$ and $n_{\vec{k}3} = \pm 1$ for these momenta values which is used in the main text.

Next, we provide an explicit expression for $|\epsilon_{\vec{k}}|$ for the square pulse protocol defined in the main text. This can be done by combining Eq. A8 with Eqs. E2, E3 and E4. A somewhat lengthy calculation yields

$$|\epsilon_{\vec{k}}| = \arccos(M_{\vec{k}})/T \qquad \text{(E5)}$$

with

$$M_{\vec{k}} = \cos(\Phi_{\vec{k}i})\cos(\Phi_{\vec{k}f}) - \hat{N}_{\vec{k}i}\cdot\hat{N}_{\vec{k}f}\sin(\Phi_{\vec{k}i})\sin(\Phi_{\vec{k}f}) \qquad \text{(E6)}$$

where $\Phi_{\vec{k}i(f)} = E_{\vec{k}i(f)}T/2$ with $E_{\vec{k}i(f)} = \sqrt{(g_{i(f)}-b_{\vec{k}})^2 + \Delta^2_{\vec{k}}}$ and the components of $\hat{N}$ are given by

$$\hat{N}_{\vec{k}i(f)} = \left(\frac{\Delta_{\vec{k}}}{E_{\vec{k}i(f)}}, 0, \frac{g_{i(f)}-b_{\vec{k}}}{E_{\vec{k}i(f)}}\right). \qquad \text{(E7)}$$

We now show how to compute ω_c, i.e. the first critical drive frequency for the dynamical phase transition as the drive frequency ω is reduced from $\omega \gg 1$ for this protocol. For simplicity, we restrict to the one dimensional case where $k \in [0, \pi]$. First, we note that a new zero in $d|\epsilon_k|/dk$ can only appear from the boundaries $k = 0, \pi$. We have numerically checked that the appearance of the first extra zero in $d|\epsilon_k|/dk$ is from $k = \pi$ for the square pulse protocol. Then, ω_c can be simply calculated by expanding $d|\epsilon_k|/dk$ for $k = \pi - \epsilon$ and finding the value of ω where the $\mathcal{O}(\epsilon)$ term first changes its sign. This leads to Eq. 26 of the main text.

[1] T. Grover, Y. Zhang, and A. Vishwanath, New J. Phys. **15**, 025002 (2013)

[2] J. Eisert, M. Cramer, and M. B. Plenio Rev. Mod. Phys. **82**, 277 (2010); L. Amico, R. Fazio, A. Osterloh, and V. Vedral Rev. Mod. Phys. **80**, 517 (2008).

[3] M. Levin and X-G Wen, Phys Rev B. **71**.045110 (2005).

[4] M. Melitski and T. Grover, arXiv:1112.5166 (unpublished); A. Kallin *et. al.*, Phys. Rev. B **84**, 165134 (2011).

[5] D. Gioev and I. Klich, Phys. Rev. Lett. **96**, 100503 (2006); M. M. Wolf, Phys. Rev. Lett. 96, 010404 (2006).

[6] L. Fidkowski Phys. Rev. Lett. **104** 130502 (2010).

[7] A. Kitaev and J. Preskill, Phys.Rev.Lett. **96** 110404 (2006); G. Vidal, J. I. Latorre, E. Rico, and A. Kitaev Phys. Rev. Lett. **90**, 227902 (2003).

[8] T. Grover, A. Turner and A. Vishwanath, Phys. Rev. B **84**, 075128 (2011).

[9] P. Calabrese and J. Cardy, J. Stat. Mech. , P 06002 (2004); C. Callan, and F. Wilczek, Phys. Lett. B **333**, 55 (1994); C. Holzhey, F. Larsen, and F. Wilczek, Nucl. Phys. B **424**, 443 (1994); X. Chen, G. Y. Cho, T. Faulkner, and E. Fradkin, arXiv:1412.3546 (unpublished); W.L. You, arXiv:1502.01854 (unpublished).

[10] M. A. Metlitski, C. A. Fuertes, and S. Sachdev, Phys. Rev. B **80**, 115122 (2009).

[11] S. Ryu and T. Takayanagi, Phys. Rev. Lett. **96**, 181602 (2006).

[12] M. Hastings, J. Stat. Mech, P08024 (2007).

[13] M. M. Wolf, F. Verstraete, M. B. Hastings, and J. I. Cirac, Phys. Rev. Lett. **100**, 070502 (2008).

[14] A. Polkovnikov, K. Sengupta, A. Silva, and M. Vengallatore, Rev. Mod. Phys. 83, 863 (2011).

[15] J. Dziarmaga, Adv. Phys. **59**, 1063 (2010).

[16] A. Dutta, G. Aeppli, B. K. Chakrabarti, U. Divakaran, T. F. Rosenbaum, and D. Sen, arXiv:1012.0653 (unpublished).

[17] M. Esposito, U. Harbola, andM.Mukamel, Rev. Mod. Phys. **81**, 1665 (2009); M. Campisi, P. Hanggi, and P. Talkner, ibid. **83**, 771 (2011).

[18] T. W. B. Kibble, J. Phys. A **9**, 1387 (1976); W. H. Zurek, Nature (London) **317**, 505 (1985); B. Damski, Phys. Rev. Lett. 95, 035701 (2005); A. Polkovnikov, Phys. Rev. B 72, 161201(R) (2005).

[19] K. Sengupta, D. Sen, and S. Mondal, Phys. Rev. Lett. **100**, 077204 (2008); S. Mondal, D. Sen, and K. Sengupta, Phys. Rev. B **78**, 045101 (2008).

[20] D. Sen, K. Sengupta, and S. Mondal, Phys. Rev. Lett. **101**, 016806 (2008); S. Mondal, K. Sengupta, and D. Sen, Phys. Rev. B **79**, 045128 (2009).

[21] See for example, L. D'Alessio, Y. Kafri, A. Polkovnikov, and M. Rigol, arXiv:150906411 (unpublished).

[22] I. Bloch, J. Dalibard, and W. Zwerger, Rev. Mod. Phys. **80**, 885 (2008).

[23] A. Das, Phys. Rev. B **82**, 172402 (2010); S. Bhattacharyya, A. Das, and S. Dasgupta, *ibid.* **86**, 054410 (2012).

[24] S. Mondal, D. Pekker, and K. Sengupta, Europhys. Lett. **100**, 60007 (2011).

[25] A. Lazarides, A. Das, and R. Moessner, Phys. Rev. Lett. **112**, 150401 (2014).

[26] M. Heyl, A. Polkovnikov, and S. Kehrein Phys. Rev. Lett. 110, 135704 (2013); L. D'Alessio and A. Polkovnikov, Ann. Phys. **333** 19 (2013).

[27] F. Pollmann, S. Mukerjee, A. G. Green, and J. E. Moore, Phys. Rev. E **81**, 020101(R) (2010); S. Vajna and B. Dora, Phys. Rev. B **91**, 155127 (2015); S. Sharma, U. Divakaran, A. Polkovnikov, and A. Dutta, arXiv: 1601.01637 (unpublished).

[28] E. Canovi, P. Werner, and M. Eckstein, Phys. Rev. Lett. **113**, 265702 (2014); M. Heyl, Phys. Rev. Lett. **113**, 205701 (2014);

[29] S. de Darkar, R. Sensarma, and K. Sengupta, J. Phys. Cond. Mat. **26**, 325602 (2014).

[30] A. Sen (De), U. Sen, and M. Lewenstein, Phys. Rev. A **72**, 052319 (2005); H. Wichterich and S. Bose, ibid. **79**, 060302(R)(2009); S. Deng, L. Viola, and G. Ortiz, *Proceeding of the 14th International Conference on Recent Progress in Many-Body Theories, Series on Advances in Many-Body Theory* Vol. 11 (World Scientific, Singapore), 2008, pp. 387397.

[31] K. Sengupta and D. Sen, Phys. Rev. A **80**, 032304 (2009).

[32] L. Cincio, J. Dziarmaga, M. M. Rams, and W. H. Zurek, Phys. Rev. A **75**, 052321 (2007).

[33] H. Kim and D. A. Huse, Phys. Rev. Lett. **111**, 127205 (2013).

[34] V. Eisert and I. Peschel, Annalen der Physik **17** 410 (2008).

[35] M. Rigol, V. Dunjko, V. Yurovskii, and M. Olshanii, Phys. Rev. Lett. **98**, 050405 (2007).

[36] S. Sachdev, *Quantum Phase Transitions* (Cambridge University Press, Cambridge, England, 1999).

[37] A. Kitaev, Ann. Phys. (NY) **321**, 2 (2006).

[38] X.-Y. Feng, G.-M. Zhang, and T. Xiang, Phys. Rev. Lett. **98**, 087204 (2007)

[39] H. Yao and X-L. Qi, Phys. Rev. Lett. **105**, 080501 (2010)

[40] H-D Chen and Z. Nussinov, J. Phys. A: Math. Theor. **41** 075001 (2008).

[41] A. H. Castro Neto, F. Guinea, N. M. R. Peres, K. S. Novoselov, and A. K. Geim, Rev. Mod. Phys. **81**, 109 (2009).

[42] M. Z. Hasan and C. L. Kane, Rev. Mod. Phys. **82**, 3045 (2010); X-LQi and S-C Zhang, Rev. Mod. Phys. **83**, 1057 (2011).

[43] M-C. Chung and I. Peschel Phys. Rev. B **64**, 064412 (2001).

[44] For 2D Kitaev model on a torus, $S_n^{\rm 2D}(l) = \sum_{k_y} S_n(l;k_y)$ where we have chosen the subsystem as in Ref.[39]. Each of these $S_n(l;k_y)$ is expected to behave like $S_n(l)$ for 1D system [Fig. 1(c)]. Thus the non-area, non-volume scaling of $S_n^{\rm 2D}(l)$ is expected to hold for 2D systems as well.

[45] M. Fagotti and F. H. L. Essler, Phys. Rev. B **87**, 245107 (2013).

[46] We note that similar features occur for sinusodal and linear ramp protocols as shown in App. B.

[47] M. Bukov, L. D'Alessio, and A. Polkovnikov, arXiv:1407.4803 (unpublised); L. D'Alessio and M. Rigol, Phys. Rev. X **4**, 041048 (2014).

[48] B. Mukherjee, A. Sen, D. Sen, and K. Sengupta, arXiv:1605.09178 (unpublished).

[49] R. Islam, R. Ma, P. M. Preiss, M. E. Tai, A. Lukin, M. Rispoli, and M. Greiner, Nature **528**, 77 (2015).

[50] L. Tarruell, D. Greif, T. Uehlinger, G. Jotzu, and T. Esslinger, Nature **483**, 302 (2012).

[51] N. V. Vitanov and B. M. Garraway, Phys. Rev. A **53**, 4288 (1996).